GEORG-AUGUST-UNIVERSITÄT
GÖTTINGEN

Fakultät für
Physik

Bachelor's Thesis

Untersuchung des Z+heavy flavour Untergrundes in der $HH \to b\bar{b}\tau^+\tau^-$ Suche am ATLAS Experiment

Investigation of Z+heavy flavour Background in the $HH \to b\bar{b}\tau^+\tau^-$ Search at the ATLAS Experiment

prepared by

Vanessa Annabelle Grauer

from Witzenhausen

at the II. Physikalischen Institut

Thesis number:	II.Physik-UniGö-BSc-2019/03
Thesis period:	15th April 2019 until 30th July 2019
First referee:	Prof. Dr. Stan Lai
Second referee:	Prof. Dr. Steffen Schumann

Abstract

In the following thesis, an analysis of the $Z \to \tau\tau+$ heavy flavour background in the $HH \to b\bar{b}\tau^+\tau^-$ channel is presented. It is based on 139.5 fb^{-1} proton-proton collision data, delivered by the LHC and recorded by the ATLAS detector at CERN, Geneva. This data covers the full Run II dataset from 2015-2018 at a centre-of-mass energy of $\sqrt{s} = 13$ TeV. The relevant background has been analysed by exploiting a $Z \to \mu\mu+$ heavy flavour control region. A normalisation factor is extracted by fraction fits, using a data-driven method. Two different Monte Carlo generators have been tested on different event selections under varying requirements.

The scale factors have been calculated to be $SF(Z + \text{heavy flavour}) = 1.25 \pm 0.02$ and $SF(t\bar{t}) = 0.99 \pm 0.01$ for events that were simulated using SHERPA. For MADGRAPH samples, the extracted scale factors are $SF(Z + \text{heavy flavour}) = 0.84 \pm 0.01$ and $SF(t\bar{t}) = 0.99 \pm 0.01$.

Zusammenfassung

Eine Analyse des $Z \to \tau\tau+$ heavy flavour Untergrunds im $HH \to b\bar{b}\tau^+\tau^-$-Kanal wird in dieser Arbeit vorgestellt. Auf der Grundlage von 139.5 fb^{-1} Proton-Proton Kollisionsdaten vom LHC, aufgenommen vom ATLAS Detektor am CERN in Genf, werden Untersuchungen angestellt. Diese Daten decken den kompletten Run II Datensatz im Zeitraum von 2015-2018, bei einer Schwerpunktsenergie von $\sqrt{s} = 13$ GeV, ab. Der relevante Untergrund wurde durch Nutzung einer $Z \to \mu\mu+$ heavy flavour Kontrollregion untersucht. Mit Hilfe von datengetriebenen Methoden wurden Normierungsfaktoren extrahiert. Dabei wurden zwei verschiedene Monte Carlo Generatoren unter verschiedenen Auswahlregeln getestet.

Diese Faktoren wurden berechnet zu $SF(Z + \text{heavy flavour}) = 1.25 \pm 0.02$ und $SF(t\bar{t}) = 0.99 \pm 0.01$ für Events, die mit SHERPA simuliert worden sind. Für MADGRAPH Proben sind die Normierungsfaktoren $SF(Z + \text{heavy flavour}) = 0.84 \pm 0.01$ und $SF(t\bar{t}) = 0.99 \pm 0.01$.

Contents

1. Introduction

The Standard Model of particle physics (SM) is one of the greatest achievements in the physical sciences. It is a sophisticated framework that describes most of the fundamental forces and laws of the constituents of matter. The electroweak theory [1] and the Higgs mechanism [2], incorporated into the SM, create a theoretical foundation for high energy particle physics. With the discovery of the W [3] and Z boson [4] in 1983 that verified the electroweak theory, and the 2012 discovery of the Higgs boson [5], many predictions of this model have been demonstrated to high success. Nonetheless, the SM fails to describe one of the fundamental forces of nature, the gravitational force, and is not able to explain all experimental observations that have been made in nature.
After the discovery of the Higgs boson, one of the open questions that remained is whether the Higgs boson exhibits self-coupling, which is predicted by the SM as well, but has yet to be observed.

In this thesis, the focus will lie on the investigation of the Z + heavy flavour background estimation as part of the $HH \rightarrow b\bar{b}\tau^+\tau^-$ search at the ATLAS experiment. This is an important part of the analysis, a precise and accurate background estimate is crucial to ensure high sensitivity of the analysis. In Chapter 2, a short summary of the theoretical background is described, followed by an overview of the experimental setup in Chapter 3. Chapter 4 will give an overview of the $HH \rightarrow b\bar{b}\tau^+\tau^-$ channel. The following Chapters 5 and 6 will be used to present the methods and the results of the background analysis which will be summarised in Chapter 7. Finally, an outlook will be given.

2. Theoretical Background

2.1. The Standard Model of Particle Physics

The SM is currently the best theoretical description for fundamental physics. It provides a description of the constituents of matter and also forces between them, although the gravitational force is not included. In Fig. 2.1, a short summary of the particles in the SM is shown. According to the SM, all matter consists of 12 spin-$\frac{1}{2}$ particles, the fermions. The group of fermions can be categorised into quarks and leptons. The quarks and leptons themselves are organised into three generations. Particles of the higher generation have a higher mass and thus are unstable. They decay into the particles of the first generation, which are the building blocks of matter. Every particle in the SM has a corresponding anti-particle, for example, the electron (e^-) has the positron (e^+) as its partner. The mediating particles, which transmit the fundamental forces, are all spin-1 gauge bosons. The mediators of the strong force, gluons (g), and the mediator of the electromagnetic force, the photon (γ), are massless, while the mediators of the weak force, $W^\pm$ and Z^0 are massive particles. The Higgs boson is a spin-0 scalar particle that arises as an excitation of the Higgs field (see Section 2.2). The SM is defined by the:

$$SU(3)_C \otimes SU(2)_L \otimes U(1)_Y$$

local gauge symmetry group. These symmetry groups describe many of the properties of the fundamental forces. The $SU(3)_C$ is the group of the strong interaction, described with the corresponding colour charge, $SU(2)_L \otimes U(1)_Y$ is the group of the electroweak sector, governed by symmetries involving the weak isospin and hypercharge respectively. This local gauge symmetry is spontaneously broken [7], which allows for the generation of W and Z boson masses (see Chapter 2.2).
The electromagnetic interaction has the simplest structure. Its mediating particle is the photon, which only couples to electrically charged particles, hence this interaction is characterised by the electric charge. The theory that describes this interaction is the theory of quantum electrodynamics (QED). In this field theory, the charged spin-$\frac{1}{2}$ particles are

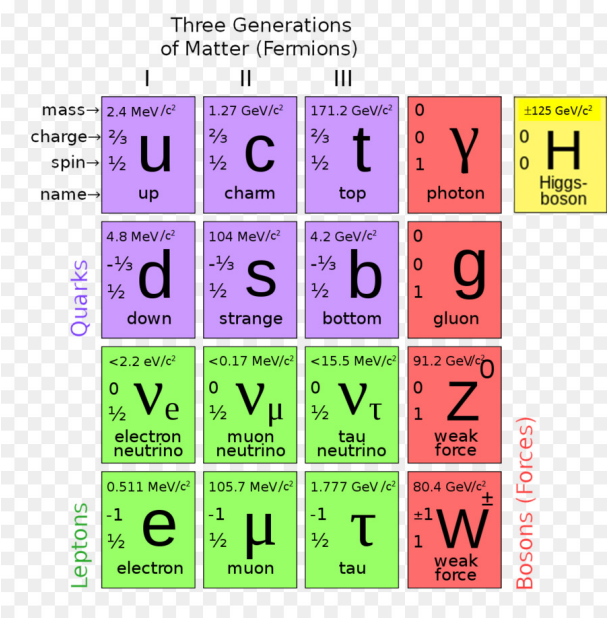

Figure 2.1.: The particles in the Standard Model. Some properties are included, e.g. the mass or the electric charge [6].

the result of an excitation of a spinor field that satisfies the Dirac equation [8]. Quantum field theory (QFT) requires the Lagrangian density [1] to be invariant under local phase transformations, i.e. under U(1) local phase transformations. This process yields the existence of a massless gauge boson (the photon) and also, as a consequence, a coupling constant α_{EM} that depends on the elementary charge. The Lagrangian describing this interaction can be written as [8]:

$$\mathcal{L}_{QED} = \bar{\psi}_n(i\gamma^\mu\partial_\mu - m_n)\psi_n - \frac{1}{4}F_{\mu\nu}F^{\mu\nu} - q_n\bar{\psi}_n\gamma^\mu A_\mu\psi_n.$$

The theory of the strong interaction is quantum chromodynamics (QCD) [9, 10], where in order to interact, the particles need a so-called colour charge, where the possibilities are red (r), blue (b) and green (g) colour. Comparable to the photon, which only couples to electrically charged particles, the gluon only couples to particles that carry colour charge. Quarks are the only fundamental fermions to have a colour charge other than zero, so they are the only fundamental fermions to interact strongly. The gluon itself carries a colour charge as well, that is why it can couple to itself in 3-point or 4-point vertices. Every baryon ($|qqq\rangle$ or $|\bar{q}\bar{q}\bar{q}\rangle$) and every meson ($|q\bar{q}\rangle$) must be in a colour-neutral state, while the combination of all colours or a combination of a colour with its corresponding

[1] Which will be referred to as the Lagrangian over the course of this thesis.

anti-colour count as neutral. This empirical phenomenon is called "colour confinement" and it can be explained by the linear term of the QCD potential:

$$V(r) = -\frac{4}{3}\frac{\alpha_s(r)}{r} + kr, \tag{2.1}$$

where α_s is the coupling constant of the strong interaction and k is a constant. In contrast to the electromagnetic interaction, where the corresponding potential is of Coulomb nature, this potential diverges for large r. Analogous to QED, QCD requires the Lagrangian to be invariant under local SU(3) gauge transformation, which corresponds to eight gluons, with eight different colour states.
The weak interaction is mediated by three massive bosons. Two of them, the W^+ and W^-, carry a flavour changing charged current. The Z boson on the other hand carries a neutral charge and according to the SM, does not directly mediate flavour changing interactions. Both bosons couple to all fermions in the SM. As mentioned earlier, these bosons are massive ($m_W = 80.4$ GeV, $m_Z = 91.2$ GeV) although the local SU(2) gauge transformation requires these gauge bosons to be massless. This problem is resolved by the mechanism of spontaneous symmetry breaking (see chapter 2.2). Another property of the weak interaction is that it is parity (P) violating, charge conjugation violating (C) and CP violating. The W boson only couples to left-handed particles or antiparticles with a right-handed chirality state.

2.2. The Higgs Mechanism

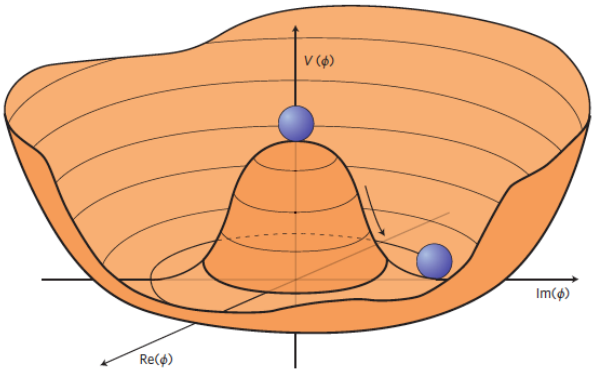

Figure 2.2.: The two-dimensional Higgs potential [11].

The need for a Higgs Mechanism arises from the fact that local gauge invariance forbids gauge bosons from having a mass. Hence, it is required to introduce the spontaneous symmetry breaking, which then leads to the prediction of the existence of the Higgs

boson. Another problem is that fermions are expected to be massless as well in order to retain the gauge invariance of SU(2). The observed physical states, however, are massive. To solve these contradictions, the Lagrangian, defined as:

$$\mathcal{L} = \frac{1}{2}(\partial_\mu \phi)(\partial^\mu \phi) - V(\phi), \tag{2.2}$$

where ϕ as a doublet of complex scalar fields:

$$\phi = \begin{pmatrix} \phi^+ \\ \phi^0 \end{pmatrix} = \frac{1}{\sqrt{2}} \begin{pmatrix} \phi_1 + i\phi_2 \\ \phi_3 + i\phi_4 \end{pmatrix}, \tag{2.3}$$

is considered. The resulting potential $V(\phi)$, known as the "Higgs-Potential" [8] forms the basis for *electroweak symmetry breaking* (EWSB). The two-dimensional form of the potential can be seen in Fig. 2.2. It is given by

$$V(\phi) = \mu^2(\phi^\dagger \phi) + \lambda(\phi^\dagger \phi)^2, \tag{2.4}$$

where μ^2 is taken to be smaller than zero and λ must be greater than zero for the potential to have a finite minimum. It can be seen that the minima are not at $\phi(x) = 0$ but at a certain *vacuum expectation value* (VEV), the actual vacuum state will either be $\langle\phi\rangle = -v$ or $\langle\phi\rangle = v$. The choice of the vacuum state breaks the symmetry of the Lagrangian spontaneously. This EWSB process yields a term for massive gauge fields when embedded into local gauge invariance.
It is possible to rewrite the complex scalar field into the "unitary gauge" by expanding the field about the VEV in order to simplify the resulting Lagrangian:

$$\phi(x) = \frac{1}{\sqrt{2}} \begin{pmatrix} 0 \\ v + h(x) \end{pmatrix}, \tag{2.5}$$

where $h(x)$ represents the physical higgs field. The Lagrangian then yields all the interaction terms between the Higgs boson with itself, e.g. the tri-linear Higgs self-coupling (defined as λ_{HHH}.[2]), and other massive gauge bosons.
Some terms in the Lagrangian can be interpreted as mass terms, e.g. the Higgs mass being:

$$m_H = \sqrt{2\lambda} v$$

[2]Note that this is a different coupling than in formula (2.4).

The resulting mass term for the $W^{\pm}$ boson can be parameterised as the following:

$$m_W = \frac{1}{2} g_W v,$$

while the Z boson mass can be expressed as

$$m_Z = \frac{1}{2} \frac{g_W}{\cos\theta_W} v.$$

g_W denotes the weak coupling constant and $\theta_W \approx 28.74°$ is the empirically measured weak mixing angle [12]. Fermion masses can be generated in the Higgs mechanism through the Yukawa coupling. The coupling of the particles with the Higgs field yields the fermion masses to be

$$m_f = \frac{1}{\sqrt{2}} g_f v,$$

where g_f is the Yukawa coupling constant. The coupling strengths of the fermions to the Higgs boson are proportional to their masses. The VEV, as a free parameter of the SM, has been measured to be $v \approx 246$ GeV [13].

2.3. The Higgs Boson Self-Coupling and Higgs-Pair Production

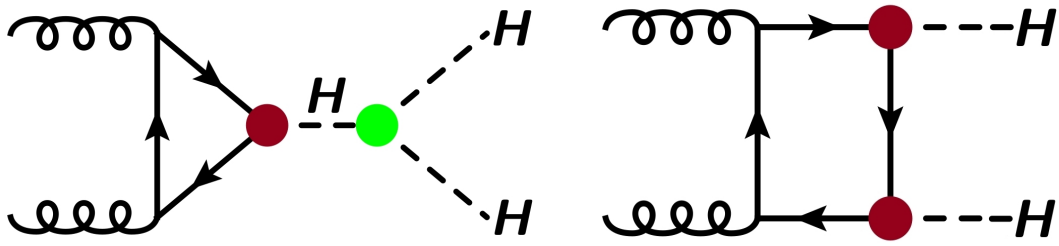

(a) Higgs boson self-coupling (b) Higgs-fermion Yukawa coupling

Figure 2.3.: Feynman diagrams for non-resonant di-Higgs production.

The Higgs boson can decay into all particles of the SM, except for the heavy top-quarks. The most promising decay channels for Higgs analyses are $H \to \gamma\gamma$, $H \to ZZ$, $H \to WW$, $H \to \tau^+\tau^-$ and $H \to b\bar{b}$. Their branching ratios (BR) can be seen in Fig. 2.4 as a function of the Higgs boson mass. The coupling of the Higgs boson is proportional to the mass of the coupled particles, which is why the Higgs boson tends to decay into fermions of the higher generations with relatively high branching ratios. This thesis will focus on the

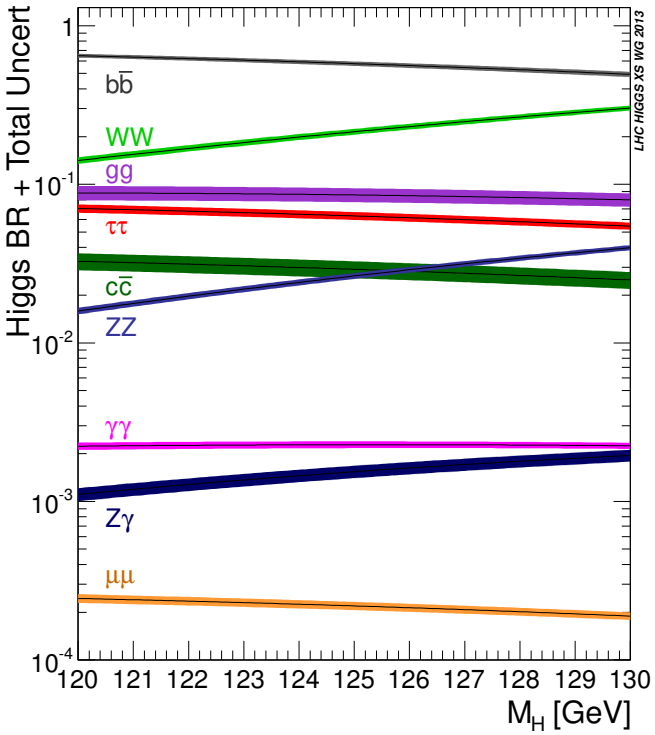

Figure 2.4.: Branching ratios for the different decay modes of the Higgs boson [14].

decay modes $H \to \tau^+\tau^-$ and $H \to b\bar{b}$. When considering the SM production of pairs of Higgs bosons, the $b\bar{b}\tau^+\tau^-$ channel is one of the most sensitive channels at the LHC **??**. The cross-section for the production of pairs of Higgs bosons is significantly lower than the cross-section for the single-Higgs boson production [15, 16]. For comparison, for the gluon-gluon Fusion (ggF) production mode, $\sigma_H = 43.92$ pb [15], while the SM expects $\sigma_{HH} = 33.45$ fb [16] for $\sqrt{s} = 13$ TeV. However, pair production and Higgs self-coupling are predicted by the SM and studies about the self-coupling are important in order to probe the shape of the Higgs potential and further test the EWSB. In Fig. 2.3(a) one can see a Feynman diagram showing the SM Higgs boson self-coupling. In Fig. 2.3(b) is a Feynman diagram depicting Higgs boson pair production via the Higgs-fermion Yukawa coupling. These diagrams interfere destructively with each other, lowering the overall production rate compared to what would be expected in the absence of the diagram in Fig. 2.3(a).

The most sensitive channels at ATLAS for Higgs pair production are $b\bar{b}b\bar{b}$, $b\bar{b}\tau^+\tau^-$ and $b\bar{b}\gamma\gamma$. The current status of di-Higgs searches at the LHC will be discussed in chapter 4.2.

3. Experimental Setup

3.1. The Large Hadron Collider

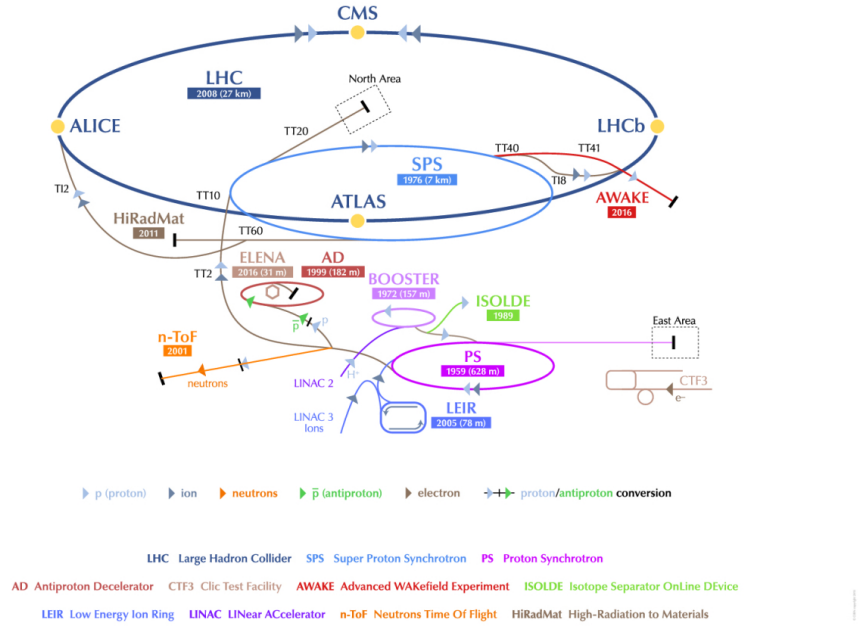

Figure 3.1.: The CERN accelerator complex [17].

The Large Hadron Collider (LHC) is the largest particle collider in the world located at CERN in Geneva, Switzerland. It is a circular proton-proton collider with 27 km in circumference and currently reaches energies up to 6.5 TeV per proton particle beam. The LHC is made of superconducting dipole and quadrupole magnets to focus the particle beam and to send the bunches of particles around the accelerator ring. There are four major experiments at the LHC - the ATLAS, CMS, LHCb and ALICE experiments. Their detectors are placed all around the accelerator ring, as indicated in Fig. 3.1. The protons get pre-accelerated by a chain of several acceleration mechanisms. First, the particles go

through Linac 2, which accelerates the protons to an energy up to 50 MeV. After that, the bunches pass the proton Synchrotron Booster (PSB) and the Proton Synchrotron. In this process, the protons acquire energies up to 25 GeV. Finally, the particles get accelerated by the Super Proton Synchrotron (SPS) which pushes the bunches to energies of 450 GeV before they get sent into the LHC. After that, the particles reach energies up to currently 6.5 TeV per particle beam.

3.2. The ATLAS Detector

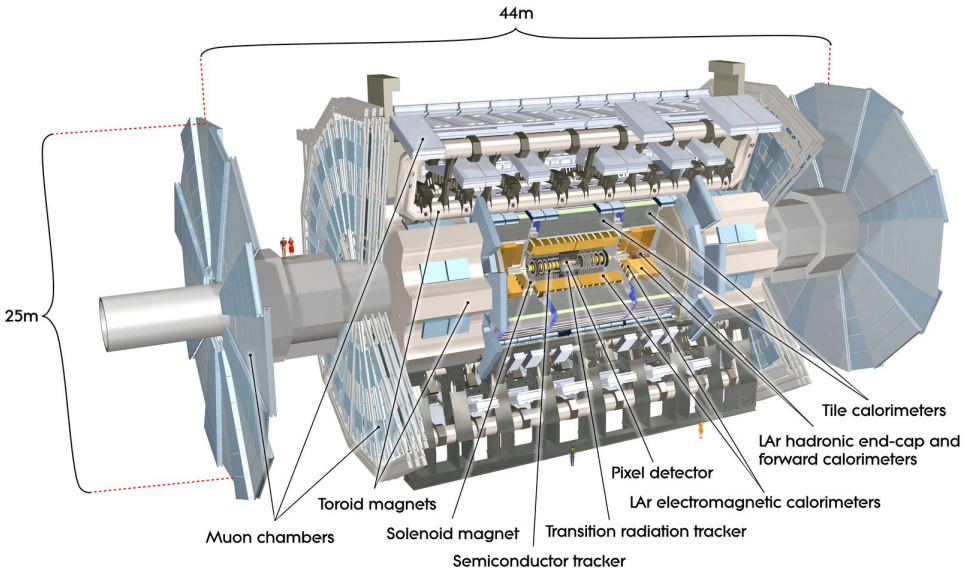

Figure 3.2.: The ATLAS detector and subsystems [18].

The ATLAS (A Toroidal LHC ApparatuS) detector is a general-purpose detector built into the LHC. It is a concentric and hermetic (= 4π coverage) multi-layer detector system around the interaction point to cover a large variety of possible particles interacting during the collisions. The setup of the detector can be seen in Fig. 3.2. ATLAS uses a hybrid superconducting magnetic system. A 2 T strong central magnetic field parallel to the beam axis is produced by a large solenoid magnet surrounding the inner detector. There are also three weaker magnets which produce a toroidal field inside the muon chambers and the end-caps of the detector with field strengths ranging from 0.5 to 1 T. The detector composition can be broken down into three major parts: The tracking detector, the calorimeter system and the muon system [19]. The ATLAS experiment uses a specific coordinate system, with the nominal interaction point as the origin of this system. The

x-axis is defined as pointing from the interaction point to the centre of the LHC ring and the positive y-axis points upwards. The beam direction defines the z-axis and the detector geometry implies that a cylindrical coordinate system is the most appropriate. The azimuthal angle ϕ goes around the beam axis and the polar angle θ is defined as the angle from the beam axis. Usually, instead of θ, a variable called the pseudorapidity is defined. The pseudorapidity is $\eta = -\ln(\tan\theta/2)$ [19]. Table 3.1 summarizes the η-coverages and resolutions of the individual detector components.

The tracking detector is used to track and vertex the path of charged particles after the collision. The magnetic field causes the particles to change their trajectory due to the Lorentz force and the tracking system localises them in space with, for example, finely segmented layers of silicon semiconductors. ATLAS uses a pixel tracker in conjunction with a silicon microstrip tracker (SCT) and a straw tube transition radiation tracker (TRT) to handle the huge experimental requirements that come from collider [19].

The Calorimeter System Calorimeters are used to slow particles down by absorbing their energy. The deposited energy is reconstructed to the incident particle and is, together with the position measurement from the tracking chamber, used to reconstruct the 4-momentum of the particle. ATLAS uses two calorimeters. The first one, the electromagnetic calorimeter (ECAL), mainly absorbs the energy through electromagnetic showers produced by electrons and photons. It is made of liquid argon (LAr) as the active and lead as the passive material and has a total thickness of > 22 radiation lengths (X_0) in the barrel and $> 24X_0$ in the end-caps. The second calorimeter is the hadronic calorimeter (HCAL), which detects hadronic showers. It is made of LAr as well. This calorimeter is a system of steel as the absorbing material and scintillating tiles as the active part of the calorimeter. It is placed directly outside the ECAL. The thickness of this calorimeter lies at around 10 interaction lengths λ. Both of them are sampling calorimeters [19].

The Muon System A highly energetic muon usually goes through the calorimeter system undetected due to its minimal ionising nature (Bremsstrahlung is suppressed). The muon chamber is an additional tracking system outside of the calorimeters to track muons. This is achieved by cathode strip chambers using resistive plate chambers for triggering in the inner layer, monitored drift tubes for precision measurements, thin gap chambers for trigger information in the outer region and cathode strip chambers, which are a specific kind of multiwire proportional chambers, to cover high pseudorapidities. The magnetic field required for tracking the particles is generated by a system of three torroidal magnets, where two of them are placed in the end-caps and one is placed in the barrel, as indicated earlier [19].

The Trigger System Another important aspect of the ATLAS detector is the imple-

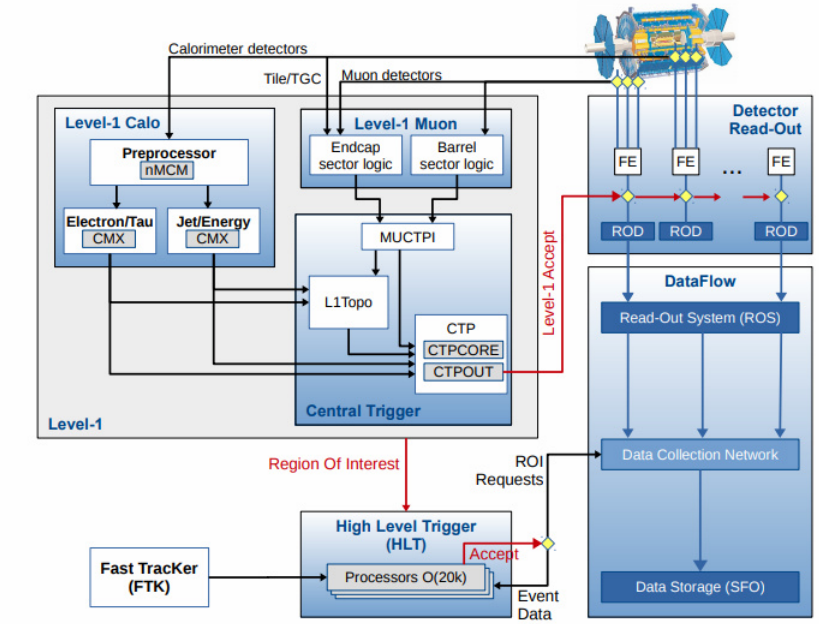

Figure 3.3.: Schematic layout of the ATLAS trigger system and data acquisition system [20].

mented trigger system. It is a multi-level trigger system designed to cope with the high luminosity that the LHC delivers. It is made of a hardware-based Level-1 (L1) and a software-based high-level trigger (HLT). These triggers are able to reduce the incoming event rate from approximately 40 MHz to around 1 kHz. The L1 reduces the event rate from 30 MHz to approximately 100 kHz with a latency of 2.5 μs. This is done by determining regions-of-interest via the readout electronics in the L1 trigger.The data is then sent to the HLT, which uses sophisticated selection algorithms to reduce the event rate further to 1 kHz. The whole event selection scheme is represented in Fig. 3.3 [20].

Detector Component	Required resolution	η coverage Measurement	η coverage Trigger
Tracker	$\sigma_{p_T}/p_T = 0.05\% p_T \oplus 1\%$	± 2.5	
EM calorimeter	$\sigma_E/E = 10\%/\sqrt{E} \oplus 0.7\%$	± 3.2	± 2.5
Hadronic calorimeter (jets)			
barrel and end-cap	$\sigma_E/E = 50\%/\sqrt{E} \oplus 3\%$	± 3.2	± 3.2
forward	$\sigma_E/E = 100\%/\sqrt{E} \oplus 10\%$	$3.1 < \lvert\eta\rvert < 4.9$	$3.1 < \lvert\eta\rvert < 4.9$
Muon spectrometer	$\sigma_{p_T}/p_T = 10\%$ at $p_T = 1$ TeV	± 2.7	± 2.4

Table 3.1.: General performance of the ATLAS detector. The units for E and p_T are in GeV [19].

4. The $HH \to b\bar{b}\tau^+\tau^-$-Channel

4.1. Motivation and Phenomenology

The main motivation for the analysis of the di-Higgs production process is the measurement of the Higgs boson self-coupling constant. The SM predicts this constant to be

$$\lambda_{HHH}^{SM} = \frac{3m_H^2}{v}, \tag{4.1}$$

with the Higgs mass $m_H = 125$ GeV and the VEV defined earlier [21]. The cross section for the SM di-Higgs production in the ggF production mode, with the destructive interference of the Feynman diagrams in Fig. 2.3 taken into account, is predicted to be 33.45 fb for $\sqrt{s} = 13$ TeV at NNLO [16]. This cross section depends on λ_{HHH}^{SM}. The LHC is not expected to be able to measure such a low cross-section with the current dataset of 139.5 fb^{-1}, but it is expected that strong upper limits on σ_{HH} can be set.
This analysis is also sensitive to enhanced cross-sections in physics beyond the Standard Model (BSM). Many BSM theories suggest that there could be a different trilinear coupling constant from processes we do not know yet. Observations consistent with the SM would result in $\frac{\lambda_{HHH}^{measured}}{\lambda_{HHH}^{SM}} \approx 1$. A deviation from this result would hint at either unknown production modes or a different interference of processes than previously predicted.
The analysis can also be designed to look for heavy resonances decaying into two SM Higgs bosons (resonant di-Higgs production). The Two-Higgs-Doublet-Model (2HDM) [22] assumes the existence of more than one Higgs boson. Adding another Higgs doublet leads to five different scalar states. The CP even neutral states are noted as h and H. The Higgs boson observed at the LHC is in a CP even state, so it can be identified as one of these scalar states. In addition to that, the theory supposes the existence of a CP odd neutral state, the A boson and two charged states of the Higgs boson, $H^\pm$.
When looking at the $HH \to b\bar{b}\tau^+\tau^-$-channel, it is often distinguished between the two different subchannels with the highest branching ratios. The first one, represented in Fig. 4.1 (a), is the $HH \to b\bar{b}\tau_{lep}\tau_{had}$-channel, where τ_{lep} corresponds to $\tau \to \mu/e + \bar{\nu}_{\mu/e}$ decay mode, while τ_{had} refers to hadronically decaying τ leptons. The second channel is the

$HH \to b\bar{b}\tau_{had}\tau_{had}$-channel, represented in Fig. 4.1 (b).

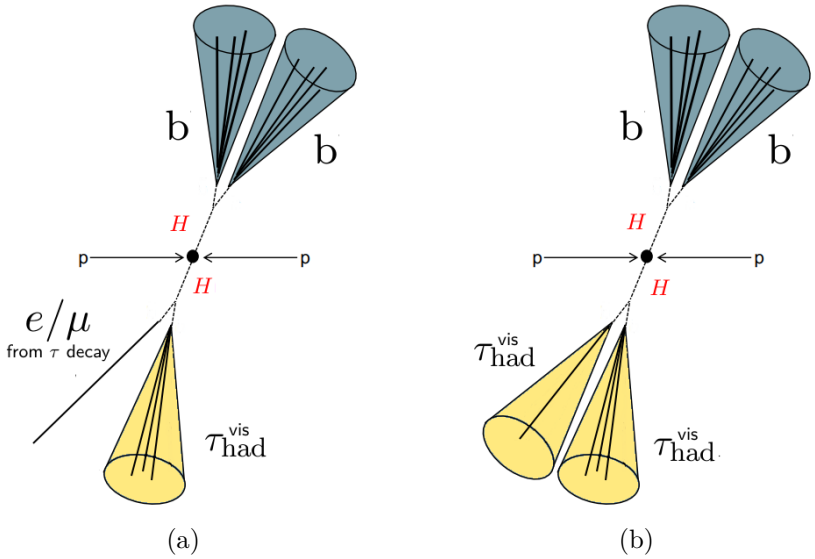

Figure 4.1.: Schematic decays of the different $HH \to b\bar{b}\tau^+\tau^-$-channels.

In the $HH \to b\bar{b}\tau^+\tau^-$-channel, the most dominant backgrounds are $t\bar{t}$, QCD-induced backgrounds, processes where quark-, or gluon-initiated jets are faking hadronically decaying taus and $Z \to \tau\tau + h.f.$ processes (see Fig. 4.2).
Monte Carlo (MC) generators are widely used in high-energy physics to simulate collision events. Together with the simulation of a detector response, they are used to estimate signals and backgrounds. These estimations are then tested against observed data. Some processes are very difficult to simulate and the uncertainties of these predictions can be very large. In those cases, whenever possible, it is favoured to use a data-driven method for background estimations. This in particular is relevant for the $Z \to \tau\tau + h.f.$ background, since a disagreement between the data and MC prediction was observed. Given that it was found to be difficult to define a pure enough $Z \to \tau\tau + h.f.$ control region (CR), the $Z \to \mu\mu + h.f.$ CR is used to constrain the $Z \to \tau\tau + h.f$ normalisation, which assumes that the normalisation of $Z + h.f.$ background does not depend on the decay mode of the Z boson. Muons are easier to identify than the hadronically decaying τ-leptons and the $Z \to \mu\mu$ final state is much cleaner than the $Z \to \tau\tau$ final state. This assumption does not account for potential acceptance differences between the $Z \to \tau\tau$ and $Z \to \mu\mu$ events, but this can be treated as a systematic uncertainty of the method.

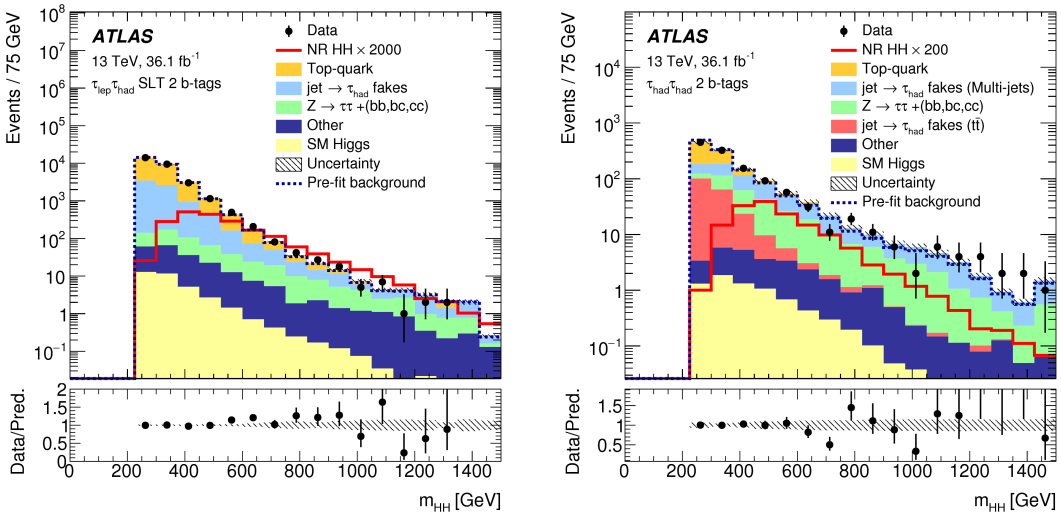

(a) $\tau_{lep}\tau_{had}$ (b) $\tau_{had}\tau_{had}$

Figure 4.2.: Reconstructed di-Higgs mass m_{HH} in the $\tau_{lep}\tau_{had}$ and the $\tau_{had}\tau_{had}$ channel for 2016 data. [23]

4.2. Current Limits on The Higgs Boson Self-Coupling

The ATLAS Collaboration published limits on the cross section for resonant and non-resonant Higgs boson pair production in the $b\bar{b}\tau^+\tau^-$ decay channel at a centre-of-mass energy of $\sqrt{s} = 13$ TeV [23]. The analysis was performed with 36.1 fb^{-1} of pp collision data delivered by the LHC, recorded in 2015 and 2016 by the ATLAS experiment. Fig. 4.2 shows the result of the reconstructed di-Higgs mass, m_{HH}, for the $\tau_{lep}\tau_{had}$ and $\tau_{had}\tau_{had}$ channels after the signal region event selection. No significant excess above the expected background was observed in the data. Upper limits of 30.9 fb are set on the non-resonant Higgs boson pair production cross section times the $b\bar{b}\tau\tau$ branching ratio, at 95% confidence level (CL) [23]. Table 4.1 summarizes the results and compares them to the theoretically expected values with uncertainties of $\pm 1\sigma$. Fig. 4.3 shows the results of the other di-Higgs searches published recently by the ATLAS collaboration, as well as the combined upper limit on the SM di-Higgs production cross section [24].
It is really important for data-driven analyses to have sophisticated knowledge about the background composition. As can be seen in Fig. 4.2, the most dominant backgrounds in the $HH \to b\bar{b}\tau^+\tau^-$ analysis are top quarks, $jet \to \tau_{had}$ fakes and $Z \to \tau\tau + h.f.$ events. In the previous analysis [23], a $Z \to \mu\mu + h.f.$ control region (CR) was used to determine the $Z \to \tau\tau + h.f.$ normalisation factor. The selection of this CR required the muon

$\sigma(HH \to bb\tau\tau)$ [fb]	Observed	-1σ	Expected	$+1\sigma$
$\tau_{lep}\tau_{had}$	57	49.9	69	96
$\tau_{had}\tau_{had}$	40.0	30.6	42.4	59
Combination	30.9	26.0	36.1	50

Table 4.1.: Observed and expected upper limits at 95% C.L. on the di-Higgs production cross-section [23].

candidates to have a $p_T > 27$ GeV with a di-muon invariant mass $m_{\mu\mu}$ between 81 and 101 GeV. To remove contributions from SM VH processes, the reconstructed di-jet mass, m_{bb}, was vetoed in the range from 80 to 140 GeV. From the combined $b\bar{b}\tau\tau$ profile likelihood fit, the scale factor was found to be 1.34 ± 0.16 for Z+ heavy flavour and 1.06 ± 0.13 for $t\bar{t}$ MC prediction[1].

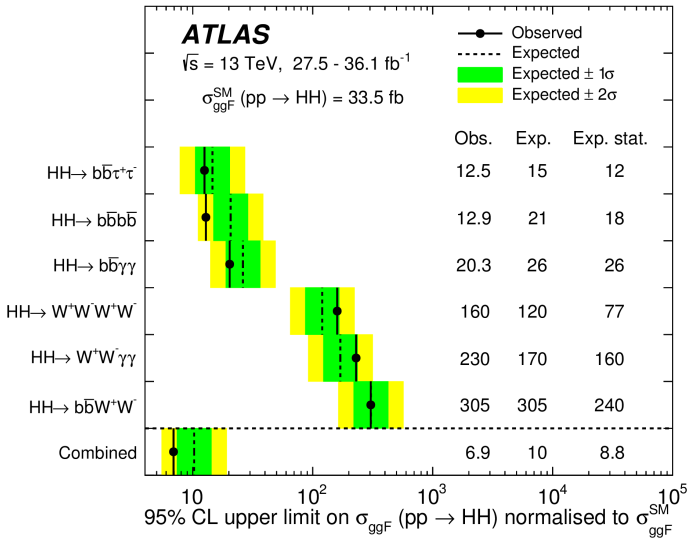

Figure 4.3.: Upper limits at 95% CL on the cross-section of the ggF SM di-Higgs production normalised to its SM expectation from the combined $b\bar{b}\tau\tau, b\bar{b}b\bar{b}, b\bar{b}\gamma\gamma, WWWW, WW\gamma\gamma$ and $b\bar{b}WW$ searches[24].

[1]Events simulated using SHERPA.

5. Estimating the $Z \to \tau^+\tau^- +$ heavy flavour background

In this chapter, a technical overview of the framework, the MC samples, and the different inputs used throughout the analysis are given. Furthermore, the event selections and yields for varying cuts are given and discussed.

5.1. The $Z \to \mu\mu + h.f.$ Control Region

For estimating the $Z \to \tau^+\tau^- + h.f.$ backgrounds, one needs to consider the reconstruction of the MC to the data in the SR. This is done by determining a CR to retrieve MC-to-data scale factors (SFs) which can be extrapolated to the SR. To determine these SFs for the $Z \to \tau^+\tau^- + h.f.$ background in the $HH \to b\bar{b}\tau^+\tau^-$ SR, the $Z \to \mu\mu + h.f.$ is considered as the CR. In the beginning, a loose event preselection is applied and several different selections are being considered, as well as a selection similar to the previous analysis [23], to better understand the dependence of the SFs on the kinematic requirements. Section 5.1.1 illustrates how the different selections are defined.
The studies presented in this thesis have been performed with the full Run 2 dataset, although the following discussions will focus on the combined 2015+16 and 2017 data, with integrated luminosities of $\int \mathcal{L}dt = 36.1$ fb^{-1} and $\int \mathcal{L}dt = 45.3$ fb^{-1} respectively. The 2018 data is discussed separately in the Appendix A.0.1.
As mentioned earlier, MC samples were used to generate background processes. The $t\bar{t}$ events were generated using Powheg-Box [25] with Pythia 8 [26]. Events of $Z + jets$ have been simulated by Sherpa 2.2.1 [27, 28], while Madgraph 5_AMc@nlo [29] is used as an alternative generator to study the acceptance differences between these MC generators. The $t\bar{t}$ background events were normalised to the NNLO+NNLL cross section and the $Z + jets$ sample was scaled to the NNLO cross-section. More details on how the other background processes were generated can be found in Ref. [23].
Fig. 5.1(a) and Fig. 5.1(b) show examples of $m_{\mu\mu}$-distributions from the 2017 dataset with two jets, where $Z + jets$ events were reconstructed with Sherpa and Madgraph,

respectively. A loose preselection has been applied in these distributions. Further details on event selections will be given in chapter 5.2. It can be clearly seen, that SHERPA underestimates, while MADGRAPH overestimates the $Z+h.f.$ contribution when compared to data, thus the need for a background normalisation. The $t\bar{t}$ MC sample however agrees well with the data. This can be seen in the tails of the distributions, where the difference of data to background reconstruction tends to zero. In these regions, the $t\bar{t}$ samples become the most significant background. Fig. 5.2 shows the distributions, where exactly

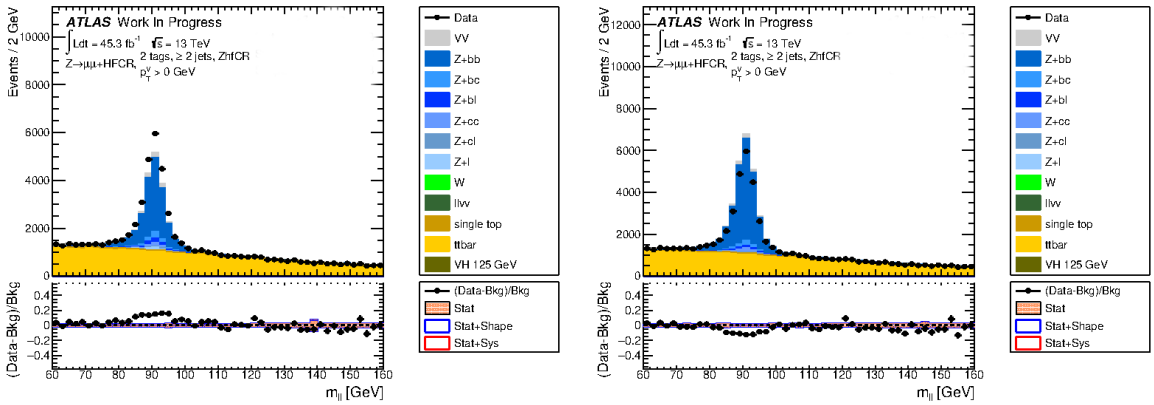

(a) SHERPA (b) MADGRAPH

Figure 5.1.: Plots of 2-tag distributions of $m_{\mu\mu}$ from 2017 data from the preselection.

zero or one jets have been identified as b-jets (0-tag and 1-tag). The 0-tag and 1-tag regions are dominated by $Z \to \mu\mu+$ light flavour and the contribution of these in regions, where exactly two jets have been identified as b-jets (2-tag), is small and described well by the MC simulation. Further considerations throughout this analysis will thus only be applied to 2-tag regions.

5.1.1. Event Selection

In this thesis, four different selections with varied cuts will be analysed. These selections are:

- Preselection
- Lephad: Selection to mimic the selection criteria of the $HH \to b\bar{b}\tau_{lep}\tau_{had}$ SR.
- Hadhad1: Selection to mimic the selection criteria of the $HH \to b\bar{b}\tau_{had}\tau_{had}$ SR for the case when the leading jet is required to have $p_T > 80$ GeV, due to the di-tau trigger design.

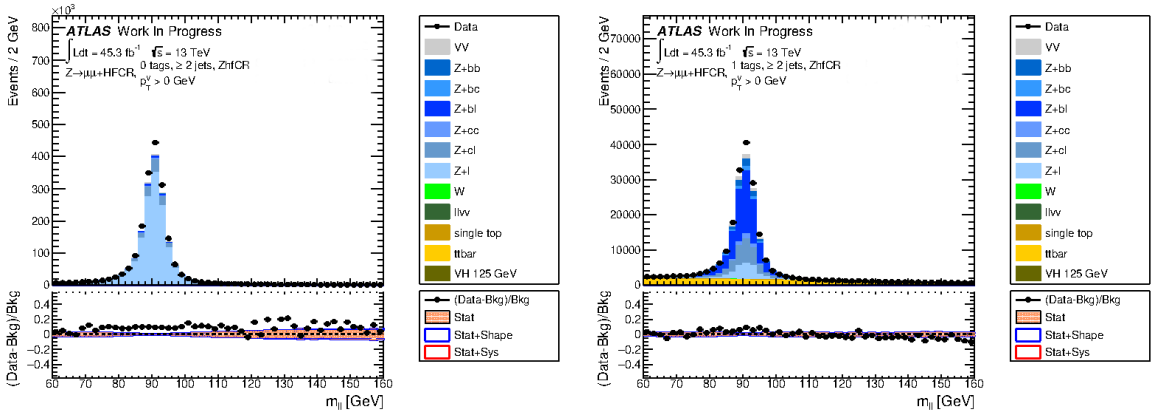

(a) 0-tag (b) 1-tag

Figure 5.2.: Plots of 0- and 1-tag distributions of $m_{\mu\mu}$ from 2017 data from the preselection.

- Hadhad2: Selection for the case when the two leading jets in the event are required to have $p_T > 45$ GeV, due to an alternative di-tau trigger design.

For all these selections, a single muon trigger is used to select events. The leading muon is required to have $p_T > 27$ GeV. Furthermore, the two muons must have opposite charge and the reconstructed di-muon mass needs to be larger than 40 GeV to cut out contributions from low energy Drell-Yan processes. A summary of the selection criteria for this *preselection* and other selections that were considered can be found in Table 5.1.
Additionally, events with 80 GeV $< m_{bb} <$ 140 GeV are vetoed. The cut on the m_{bb} is considered to ensure orthogonality to other di-Higgs analyses SRs, for instance $HH \to b\bar{b}\ell\ell$. This veto has been applied for all selections.

Throughout the course of this analysis, other cuts have been considered as well, to

Variable cuts (units in GeV)	$\mu_0^{p_T}$	$\mu_1^{p_T}$	$J_0^{p_T}$	$J_1^{p_T}$
Preselection	27	7	45	20
Lephad like Analysis	27	27	45	20
Hadhad1	60	45	80	20
Hadhad2	60	45	45	45

Table 5.1.: Summary of the different event selections used in this analysis. The different variables describe the tranverse momenta of the involved particles in GeV, i.e. $\mu_0^{p_T}$ is the momentum of the leading particle, whereas $J_0^{p_T}$ is the momentum of the leading jet.

enhance the purity of the $Z + h.f.$ CR. Fig. 5.3 shows the distribution of the missing

transverse energy E_T^{miss}. To achieve a higher purity, i.e. to reduce backgrounds other than $Z + h.f.$, E_T^{miss} provides a good discriminant against $t\bar{t}$ events. All events with $E_T^{miss} > 50$ GeV are removed from the CR.
Another variable that was analysed is the reconstructed transverse mass between a lepton and E_T^{miss}. This variable is defined as [23]:

$$M_T(\ell, E_T^{miss}) = \sqrt{2p_T^{\ell} E_T^{miss}(1 - \cos(\Delta\phi_{\ell,E_T^{miss}}))}. \tag{5.1}$$

The distribution for M_T can be seen in Fig. 5.4. Above the value of 120 GeV, the $t\bar{t}$-background becomes dominant. This is where the MC prediction agrees well with data, as $Z + h.f.$ contribution becomes negligible. Table 5.2 lists the event yields for different selections and cuts applied for an integrated luminosity of 45.3 fb^{-1}. Comparing the resulting yields after applying the E_T^{miss} and the M_T cuts, it can be seen that the M_T cut does not provide additional separation when the E_T^{miss} cut is already applied. Hence, only the E_T^{miss} cut has been applied in the analysis. After the specification of the event selections, the distributions need to be normalised to the data. In this thesis, it is done by applying template fits, which will be further discussed in the following chapter.

Event Yields	Zbb	Zbc	Zcc	$t\bar{t}$
Preselection	13536±71	1087 ±24	607±48	65248±130
$+E_T^{miss}$	11575 ±69	917±23	533 ± 47	19929±72
$+M_T$	12012± 70	965± 23	555 ± 48	44323 ± 107
$+m_{bb}$	9251 ± 57	707 ± 18	414± 39	46802 ± 111
LepHad	9450±59	766± 19	406±38	45518 ± 109
$+E_T^{miss}$	8046±57	647±19	352 ±37	14880 ± 63
$+E_T^{miss}+M_T$	5135 ± 45	386 ± 14	237 ±30	9828 ±51
$+E_T^{miss} + m_{bb}$	5412±46	410 ±14	249±31	10578 ±53

Table 5.2.: Yields from Z+h.f. and $t\bar{t}$ events in two different regions from 2017 data.

5.2. Template Fits

To obtain the $Z \to \mu\mu + h.f.$ scale factor, a template fit to data was performed in the CR, using the TFraction fitter Root class [30]. These fits have been performed on $m_{\mu\mu}$ distributions. Table 5.3 shows how the backgrounds were assigned to the two templates, namely the *Zbb*-Template and the $t\bar{t}$-Template. Other backgrounds can be neglected in further considerations. The fits are performed only in the region, where exactly two b-tagged jets are required. The TFractionFitter takes both data and MC statistical uncertainties

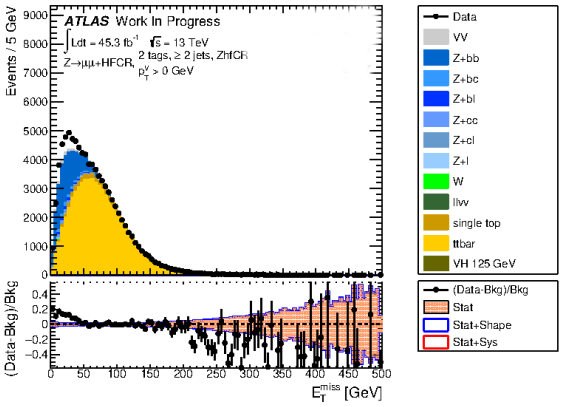

Figure 5.3.: Distribution of the E_T^{miss} for 2017 data on preselection level(2-tag).

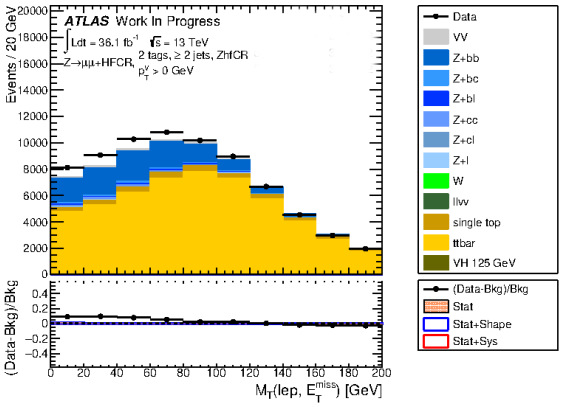

Figure 5.4.: Distribution of the M_T for 2015+16 data on preselection level(2-tag).

into account. This is the error that is shown on the plots. Fig. 5.5 shows an example of a $m_{\mu\mu}$-distribution for 2017 data, at the preselection level. The corresponding MC generator used to generate $Z + h.f.$ events in this plot is SHERPA. Chapter 6 summarises the results of these fits for different configurations.

Template	Background
Zbb	$Z + bb$, $Z + bc$, $Z + cc$
$t\bar{t}$	$t\bar{t}$, single top, Z+ light flavour, $W + jets$,...

Table 5.3.: Background selection for the two template fits. The dots indicate that the rest of the background that are less dominant are added to the $t\bar{t}$ background.

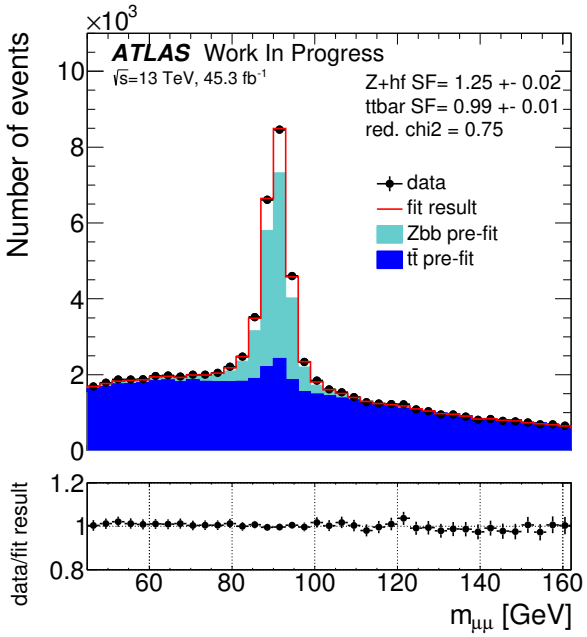

Figure 5.5.: Example plot of the template fit for 2017 data at the preselection level. This fit has 81 degrees of freedom.

6. Results of the Background Estimate

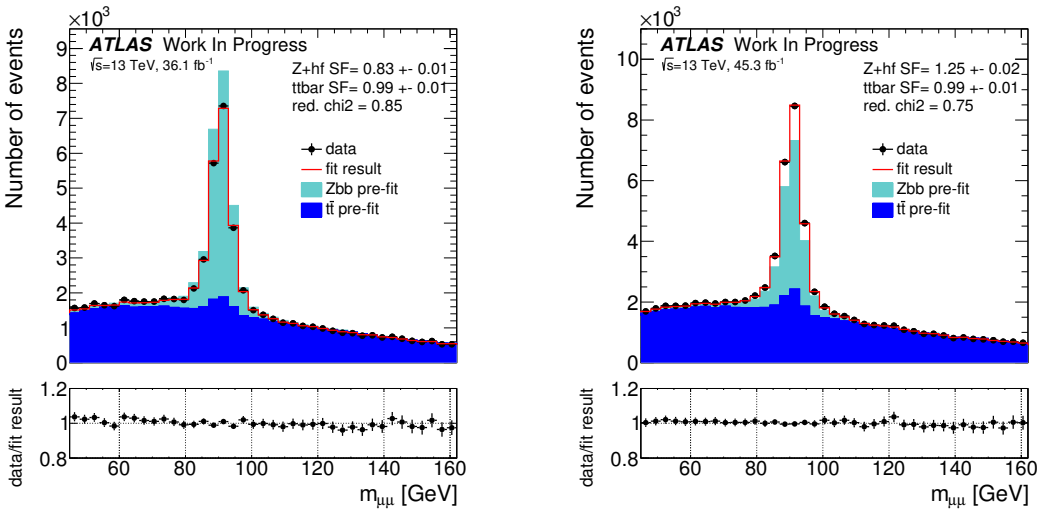

(a) 2015+16 - SHERPA

(b) 2017 - SHERPA

Figure 6.1.: Results of the fit to the 2015-2017 data for the case, where SHERPA was used to simulate events

The summary of the scale factors of the $Z + h.f.$ background, that are obtained by performing the template fit, as described in Section 5.2, is given in Table 6.1, for the case when the SHERPA MC generator is used for simulating Z+jets events and Table 6.2 for the case when the MADGRAPH MC generator was used.

Fig. 6.1 displays the fits done at preselection level of 2015+16 and 2017 data, respectively. The templates are well modelled to the data in these fits. The fit results generally agree quite well with the data points. Furthermore, the calculated scale factors are consistent throughout the years. The SF for 2017 data for SHERPA only deviates from the 2015+16 SF by 0.8%. Similar results can be seen in Fig. 6.2 for MADGRAPH samples, for 2015+16 and 2017 data, respectively. As indicated earlier, SHERPA tends to underestimate the $Z + h.f.$ prediction and thus the background prediction of $Z + h.f.$ needs to be scaled

up by 25%, while MADGRAPH overestimates the prediction. Here, the prediction must be scaled down by 16%.

Cutflow	Preselection	Lephad	Hadhad1	Hadhad2
No cut	1.25± 0.02	1.25± 0.02	1.24± 0.05	1.33± 0.06
E_T^{miss}	1.26± 0.02	1.27± 0.02	1.29± 0.05	1.38± 0.07
m_{bb}	1.30 ± 0.02	1.31± 0.03	1.31± 0.06	1.38± 0.07
$E_T^{miss} + m_{bb}$	-	1.33± 0.03	1.37± 0.06	1.42± 0.08

Table 6.1.: Summary of extracted scale factors from the *Zbb*-template, where SHERPA was used to reconstruct the events.

Cutflow	Preselection	Lephad	Hadhad1	Hadhad2
No cut	0.84± 0.01	0.84± 0.01	0.88± 0.03	0.89± 0.04
E_T^{miss}	0.83± 0.01	0.83± 0.01	0.86± 0.03	0.88± 0.04
m_{bb}	0.87 ± 0.01	0.87± 0.02	0.93± 0.04	0.93± 0.04
$E_T^{miss} + m_{bb}$	-	0.86± 0.02	0.91± 0.04	0.90± 0.04

Table 6.2.: Summary of extracted scale factors from the *Zbb*-template, where MADGRAPH was used to reconstruct the events.

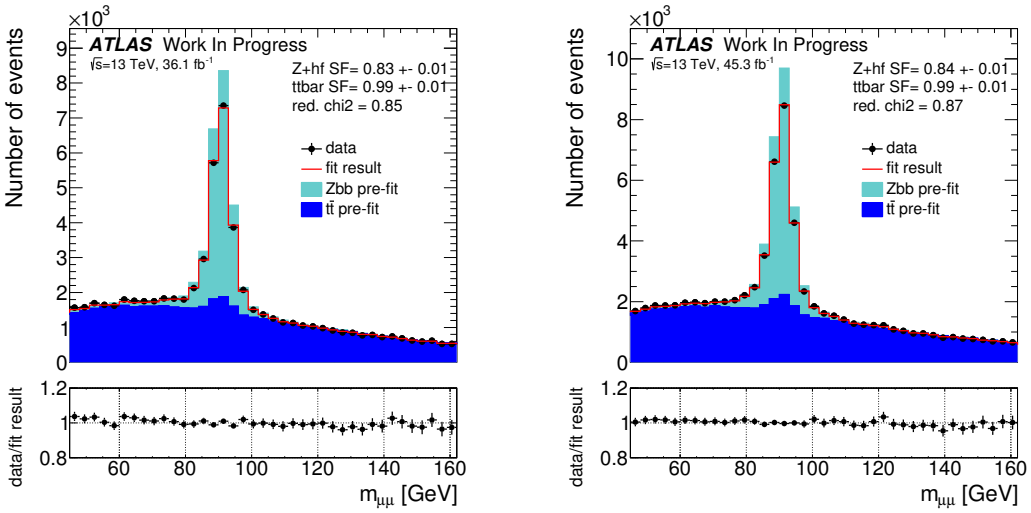

(a) 2015+16 - MADGRAPH

(b) 2017 - MADGRAPH

Figure 6.2.: Results of the fit to the 2015-2017 data for the case, where MADGRAPH was used to simulate events

Fig. 6.3 shows the fraction fits for the Lephad and Hadhad1 selection, as well as the Hadhad2 selection. These distributions were simulated by SHERPA. Both Hadhad selections

cut out a lot of $Z + h.f.$ events due to the high values of the lepton p_T cuts, especially for the Hadhad2 distribution in Fig. 6.3(c). The scale factor changes for different selections, thus it is important to later consider extrapolation uncertainties when the scale factor is applied in different signal regions. The corresponding plots for MADGRAPH can be found in Fig A.4.

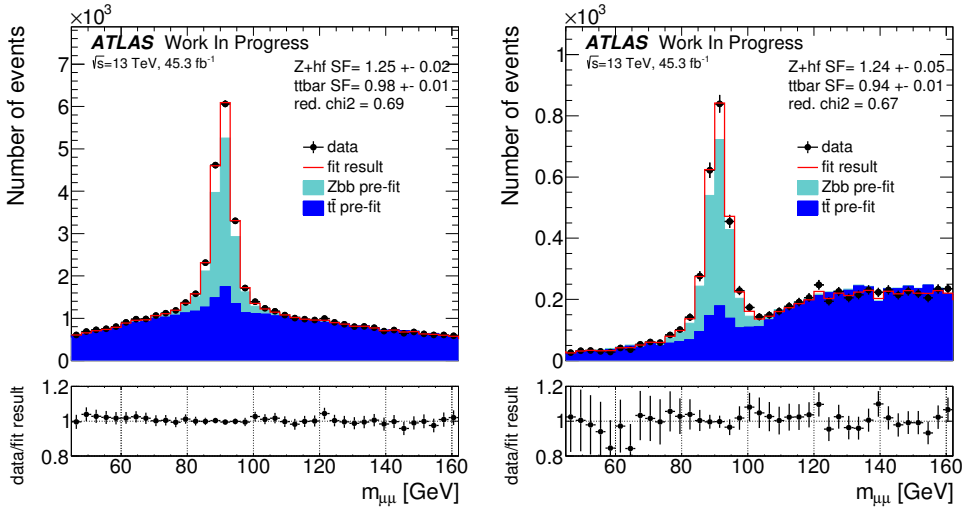

(a) Lephad (b) Hadhad1

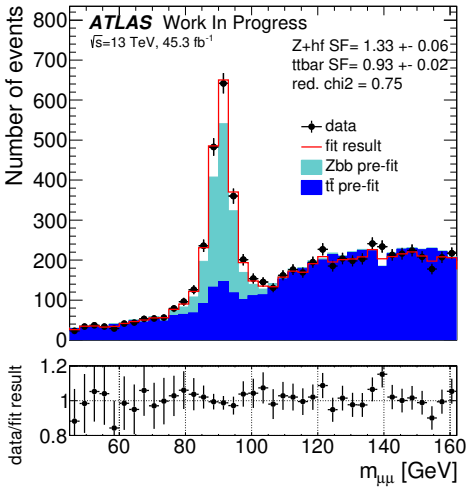

(c) Hadhad2

Figure 6.3.: Results of the fit to the 2017 data for varying selections. The MC generator used here is SHERPA.

In Fig. 6.4 the distributions for the Lephad selection for varied cuts can be seen. These fits have been performed on 2017 data with SHERPA samples. It can be seen, that the E_T^{miss} cut in (a) filters out a large fraction of $t\bar{t}$-background, while the number of $Z+h.f.$ events is not significantly affected. This provides a region with high purity. In Fig. 6.4(b) and (c) on the other hand, the m_{bb} and $E_T^{miss}+m_{bb}$ cuts remove a large fraction of $Z+h.f.$ events.
The fits that have been performed for the different selections with MADGRAPH samples can be seen in Fig. A.5 in the Appendix.
Finally, different variables have been rescaled with the scale factor extracted by performing a fit at the preselection level, for both the Zbb and $t\bar{t}$-templates. Fig. 6.5 shows an example of the variables $m_{\mu\mu}$, E_T^{miss} and M_T with the Lephad selection applied, that have been rescaled with $SF(Z+h.f.) = 1.25$ and $SF(t\bar{t}) = 0.99$. These SFs hae been obtained in the loose preselection analysis. It can be seen, that the MC prediction, after rescaling, exhibits good agreement with the data. The same conclusion can be made about Hadhad1 and Hadhad2. Fig A.6 shows the corresponding plots on Lephad selection level, where MADGRAPH was used.

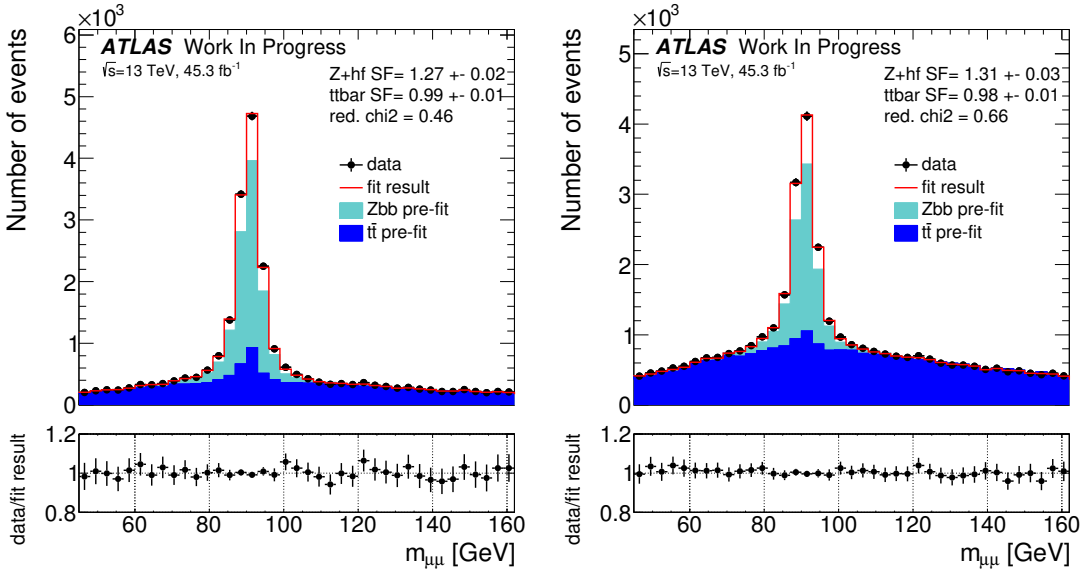

(a) E_T^{miss} cut applied

(b) m_{bb} cut applied

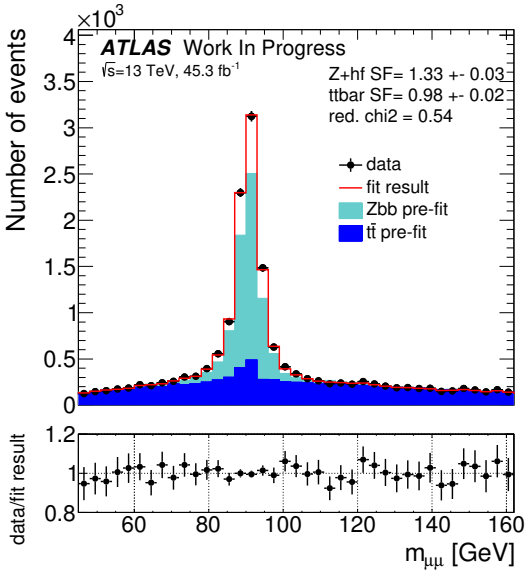

(c) $E_T^{miss} + m_{bb}$ cut applied

Figure 6.4.: Results of the fit to the 2017 data for the Lephad selection, where three different cuts were applied. The MC generator used here is SHERPA.

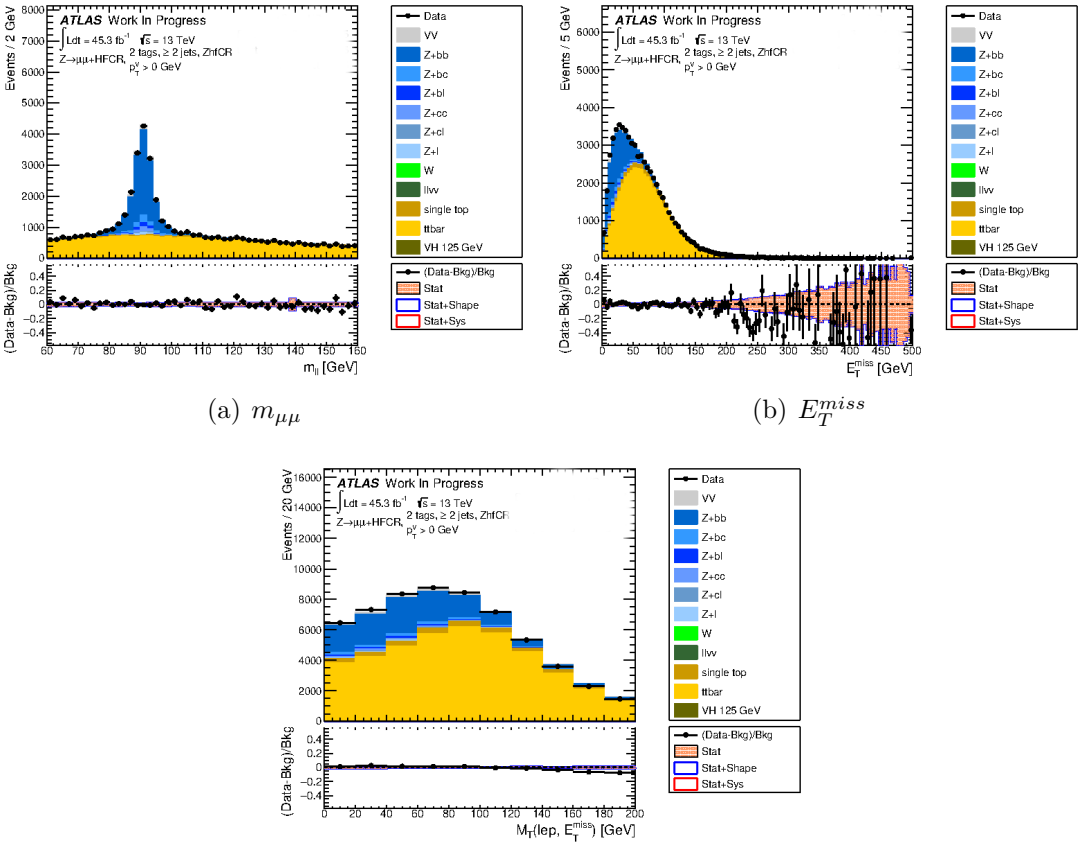

(a) $m_{\mu\mu}$ (b) E_T^{miss}

(c) M_T

Figure 6.5.: Different variables plotted from Lephad event selection. These plots have been rescaled with $SF(Zbb) = 1.25$ and $SF(t\bar{t}) = 0.99$. The MC used to simulate $Z + h.f.$ events is SHERPA.

7. Conclusion and Outlook

A data-driven normalisation for the $Z \to \tau\tau + h.f.$ background using the $Z \to \mu\mu + h.f.$ CR for the Run II collision data recorded by the ATLAS experiment at the LHC from 2015-2018 at a centre-of-mass energy of $\sqrt{s} = 13$ GeV has been investigated. The scale factor for the prediction of the SHERPA MC generator was calculated to be 1.25 ± 0.02 based on a loose preselection. For MADGRAPH, the scale factor was derived to be 0.84 ± 0.01. Note that this error is only a statistical error from the template fit. The calculated scale factor for the $t\bar{t}$-background scales down the events by 1%. The results are consistent for all the data from 2015-2017.

To implement this correction to the $Z \to \tau\tau + h.f.$ background estimate, the next step would be a full systematic treatment of these estimates. Comparisons between different MC generators are important to derive systematic uncertainties. Furthermore, acceptance differences between the MC generators need to be calculated and extrapolation uncertainties between the selections need to be derived. Finally, a profile likelihood fit of the scale factor for the chosen selection will be performed on the CR. The observation of inconsistencies in 2018 data and the MC samples simulating the events need further investigation. Evidently, this inconsistency appears only for SHERPA samples, so this is assumed to arise from a technical issue related to proccessing the sample, rather than a problem with the SHERPA generator.

The high-lumi LHC is expected to deliver 3000 fb^{-1} of data at the centre-of-mass energy of $\sqrt{s} = 14$ TeV, compared to roughly 150 fb^{-1} data from the full Run II dataset. With this amount of data, the modelling of different processes will be further improved as well as the experimental object-identification techniques. It can be expected, that searches for di-Higgs production become sensitive to non-resonant searches or even heavy resonances to open the door to new physics in the high-lumi LHC era.

A. Appendix

A.1. 2018 Data

Figure A.2 shows an example of a $m_{\mu\mu}$-distribution from the 2018 dataset with the preselection for 0-, 1- and 2-tag. The $Z \to \mu\mu + h.f.$ events have been simulated by SHERPA. The agreement between data and background reconstruction is remarkably lower than for 2015+16 or 2017 data. In Fig. A.1, it can be seen that the SF for 2016 data has been calculated to be 1.26 ± 0.02, while the SF for 2018 data is 2.06 ± 0.03. After further investigations, this inconsistency could not be explained.

However, when comparing the results for 2016 and 2018 data in Fig A.3 for MADGRAPH,

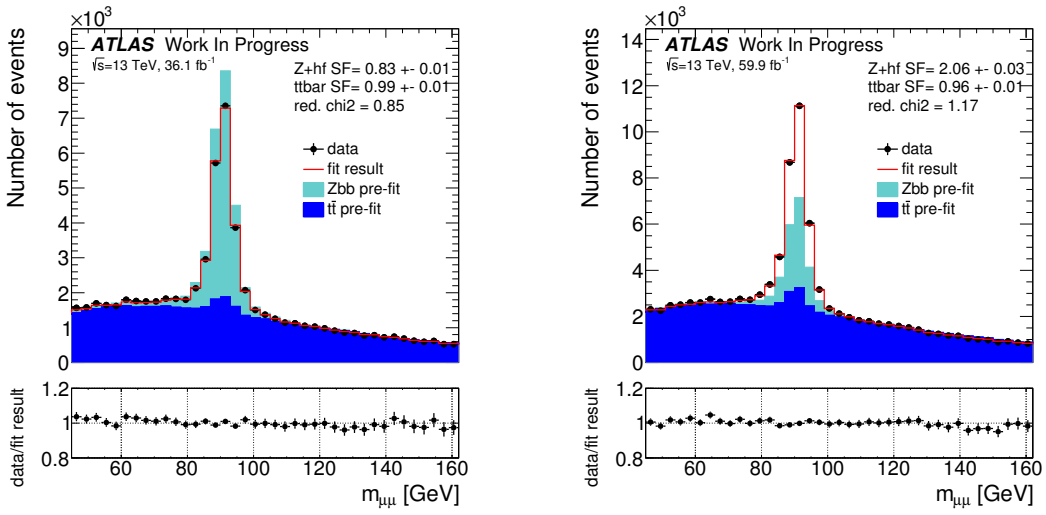

(a) 2016 (b) 2018

Figure A.1.: Comparison of fits from 2015+16 and 2018 data. SHERPA was used to reconstruct $Z + h.f.$ events.

the 2018 SF only varies by approximately 3.5% from the 2016 SF. Therefore, this inconsistency seems to arise for only for SHERPA samples. It is assumed, that this issue is of a technical nature and out of the scope of these studies. Further investigations on this topic will need to be pursued.

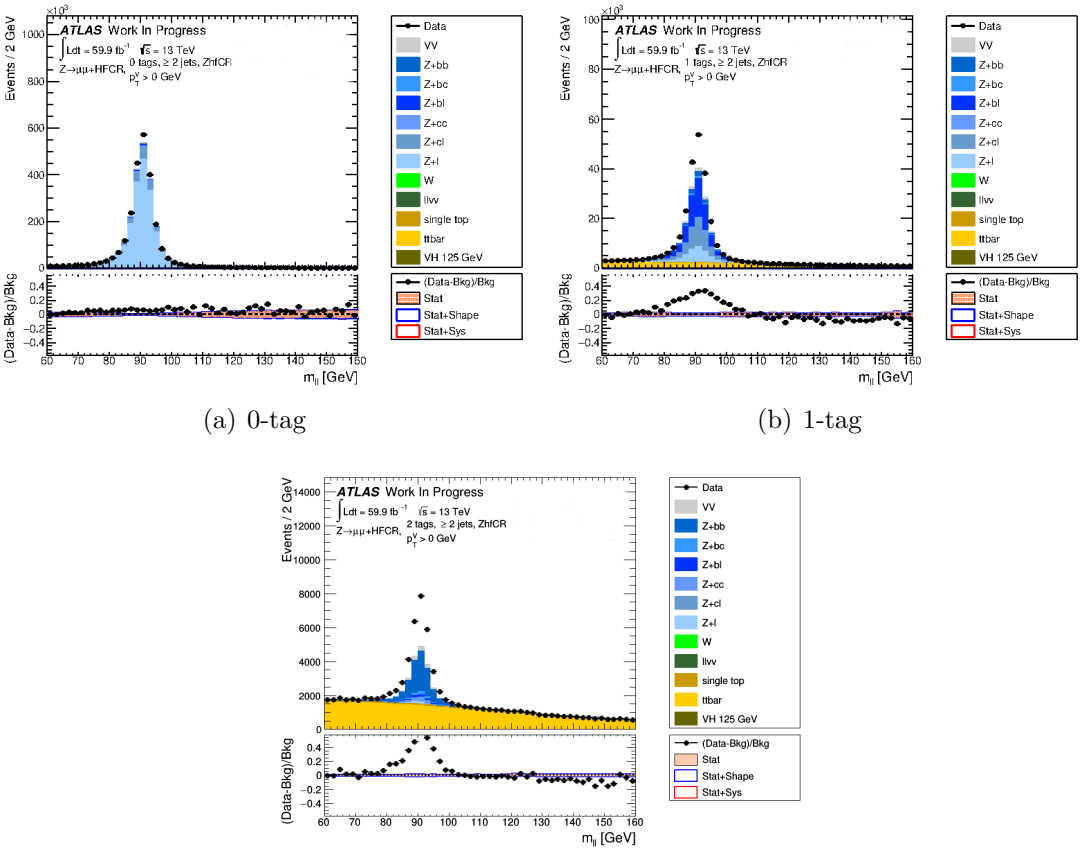

(a) 0-tag

(b) 1-tag

(c) 2-tag

Figure A.2.: Distributions of $m_{\mu\mu}$ from the preselection for different b-tag regions. The 2018 dataset was used.

A.2. Further Plots and Tables

Cutflow	Preselection	Lephad	Hadhad1	Hadhad2
No cut	0.99± 0.01	0.98± 0.01	0.94± 0.01	0.93± 0.02
E_T^{miss}	1.00± 0.01	0.99± 0.01	0.96± 0.03	0.96± 0.03
m_{bb}	1.00 ± 0.01	0.98± 0.01	0.93± 0.02	0.92± 0.02
$E_T^{miss} + m_{bb}$	-	0.98± 0.02	0.95± 0.03	0.94± 0.03

Table A.1.: Summary of extracted scale factors from the $t\bar{t}$-template, where SHERPA was used to reconstruct the events.

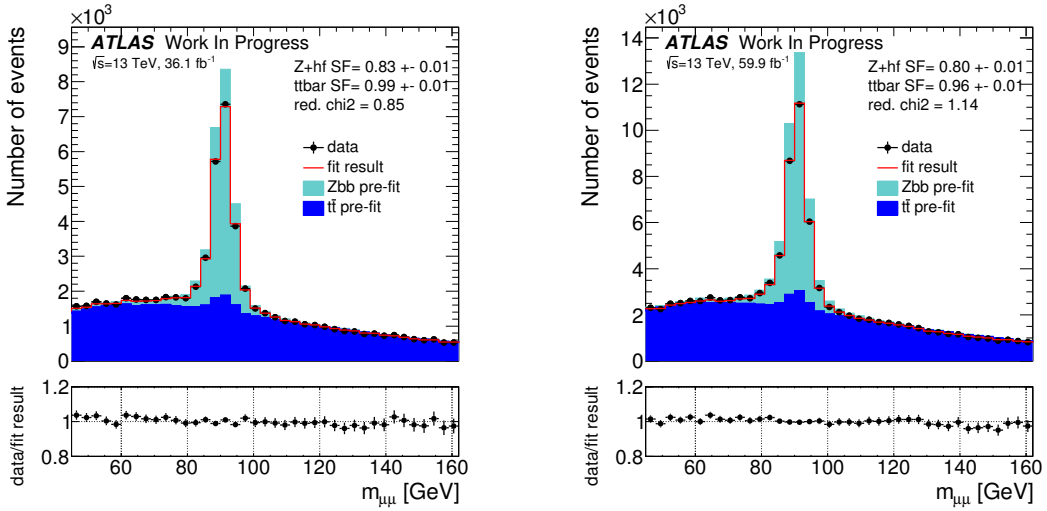

(a) 2016 (b) 2018

Figure A.3.: Comparison of fits from 2015+16 and 2018 data. MADGRAPH was used to reconstruct $Z + h.f.$ events.

Cutflow	Preselection	Lephad	Hadhad1	Hadhad2
No cut	0.99± 0.01	0.98± 0.01	0.93± 0.03	0.93± 0.02
E_T^{miss}	1.01± 0.01	0.99± 0.01	0.96± 0.03	0.96± 0.03
m_{bb}	0.99 ± 0.01	0.98± 0.01	0.93± 0.02	0.92± 0.02
$E_T^{miss} + m_{bb}$	-	0.99± 0.02	0.95± 0.03	0.94± 0.03

Table A.2.: Summary of extracted scale factors from the $t\bar{t}$-template, where MADGRAPH was used to reconstruct the events.

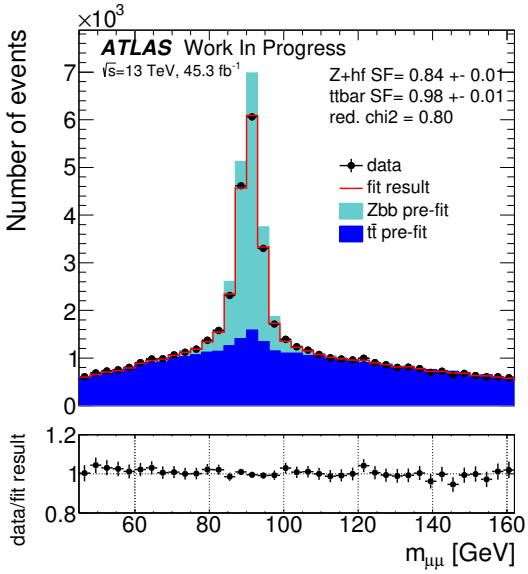

(a) Lephad

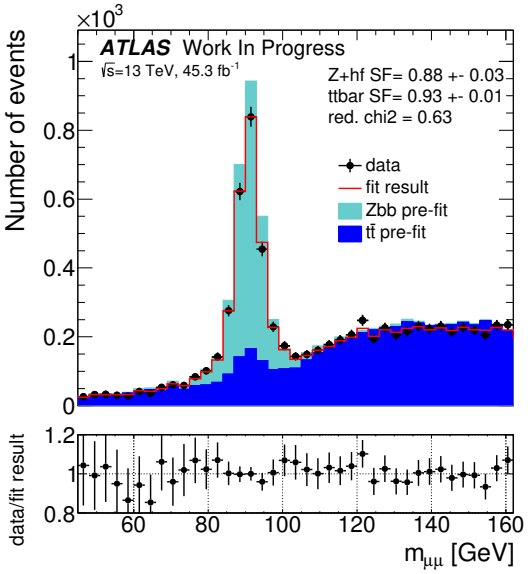

(b) Hadhad1

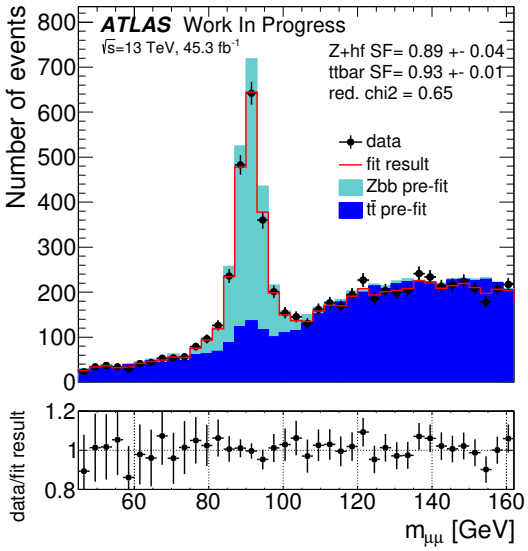

(c) Hadhad2

Figure A.4.: Results of the fit to the 2017 data for varying selections. The MC generator used here is MADGRAPH.

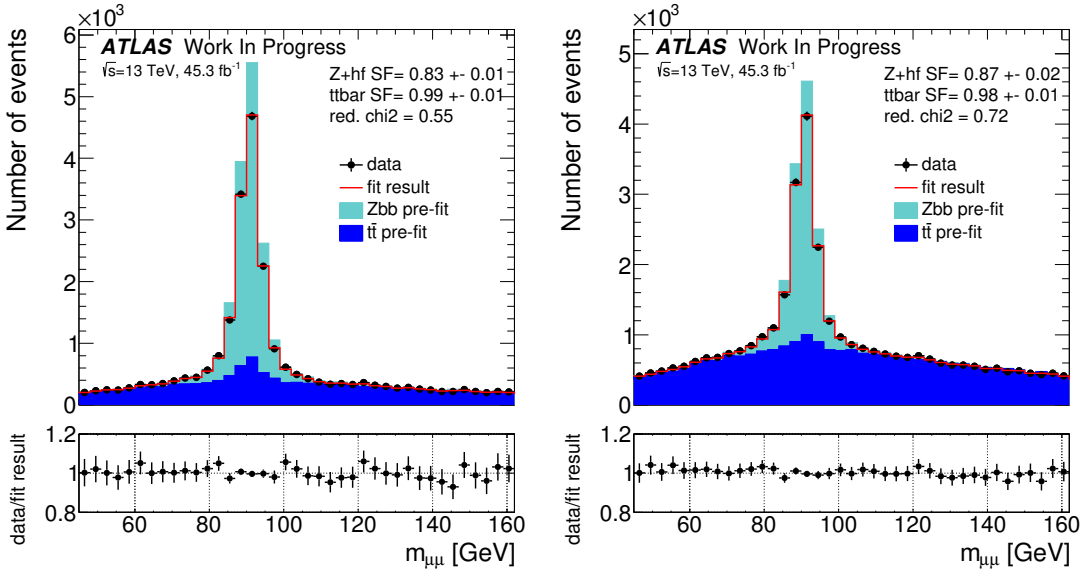

(a) E_T^{miss} cut applied

(b) m_{bb} cut applied

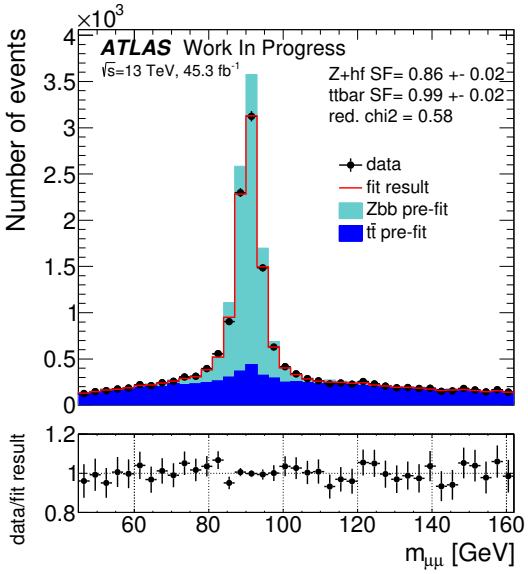

(c) $E_T^{miss} + m_{bb}$ cut applied

Figure A.5.: Results of the fit to the 2017 data for the Lephad selection, where three different cuts were applied. The MC generator used here is MADGRAPH.

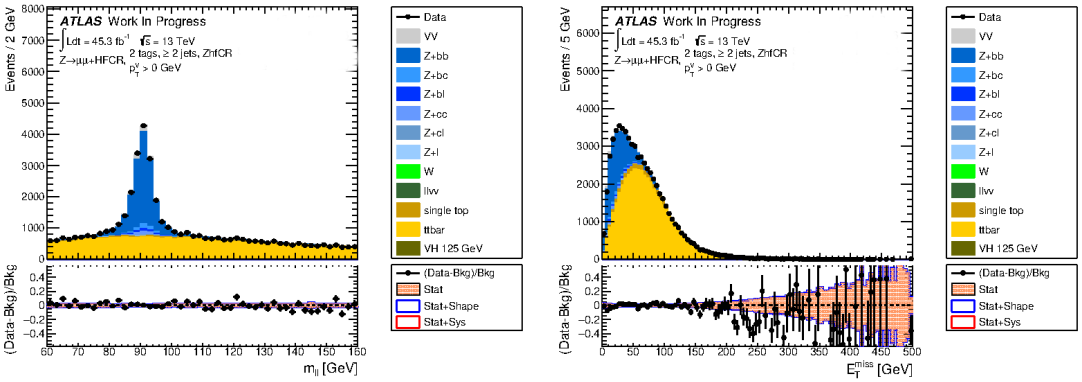

(a) $m_{\mu\mu}$ (b) E_T^{miss}

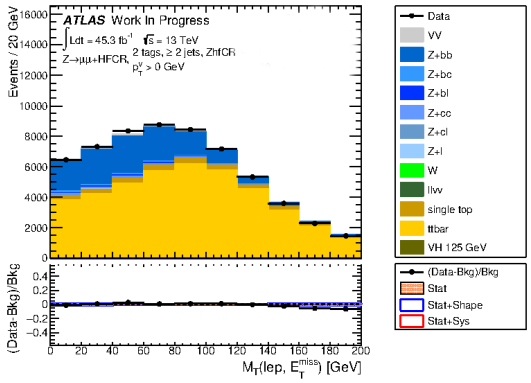

(c) M_T

Figure A.6.: Different variables plotted from Lephad event selection. These plots have been rescaled with $SF(Zbb) = 0.84$ and $SF(t\bar{t}) = 0.99$. The MC used to simulate $Z + h.f.$ events is MADGRAPH.

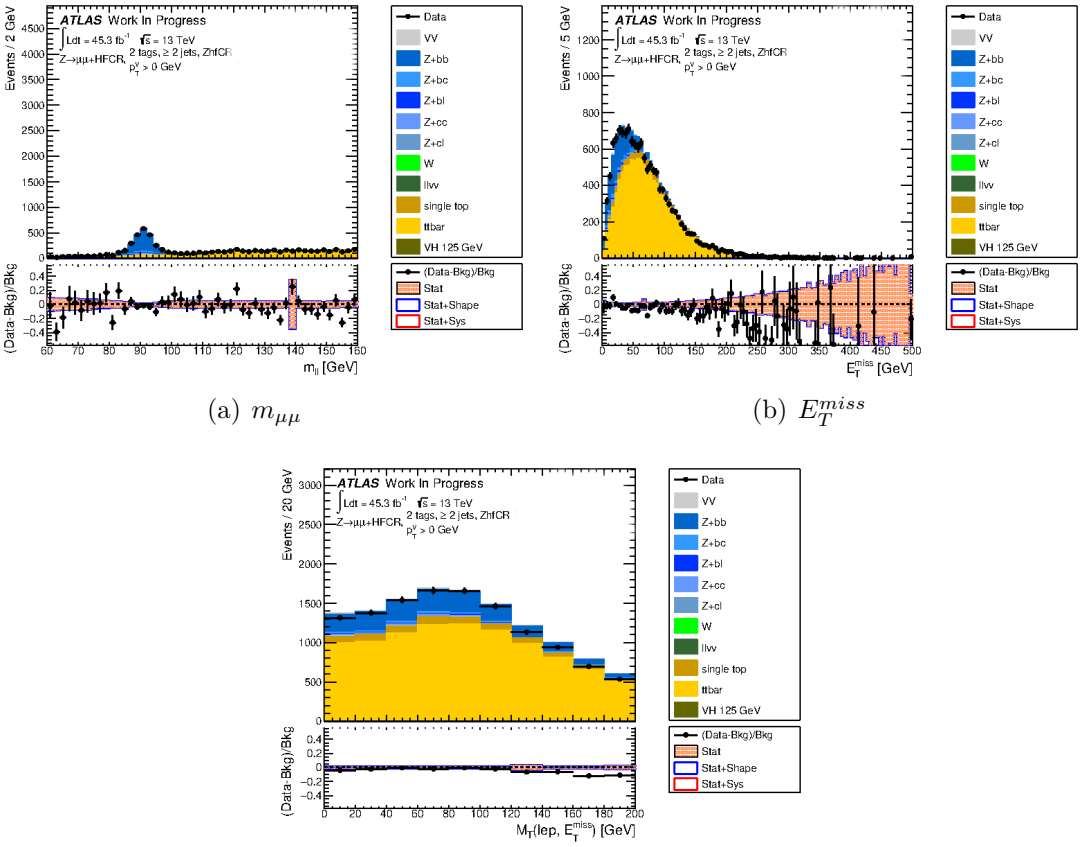

(a) $m_{\mu\mu}$

(b) E_T^{miss}

(c) M_T

Figure A.7.: Different variables plotted from Hadhad1 event selection. These plots have been rescaled with $SF(Zbb) = 1.25$ and $SF(t\bar{t}) = 0.99$. The MC used to simulate $Z + h.f.$ events is SHERPA.

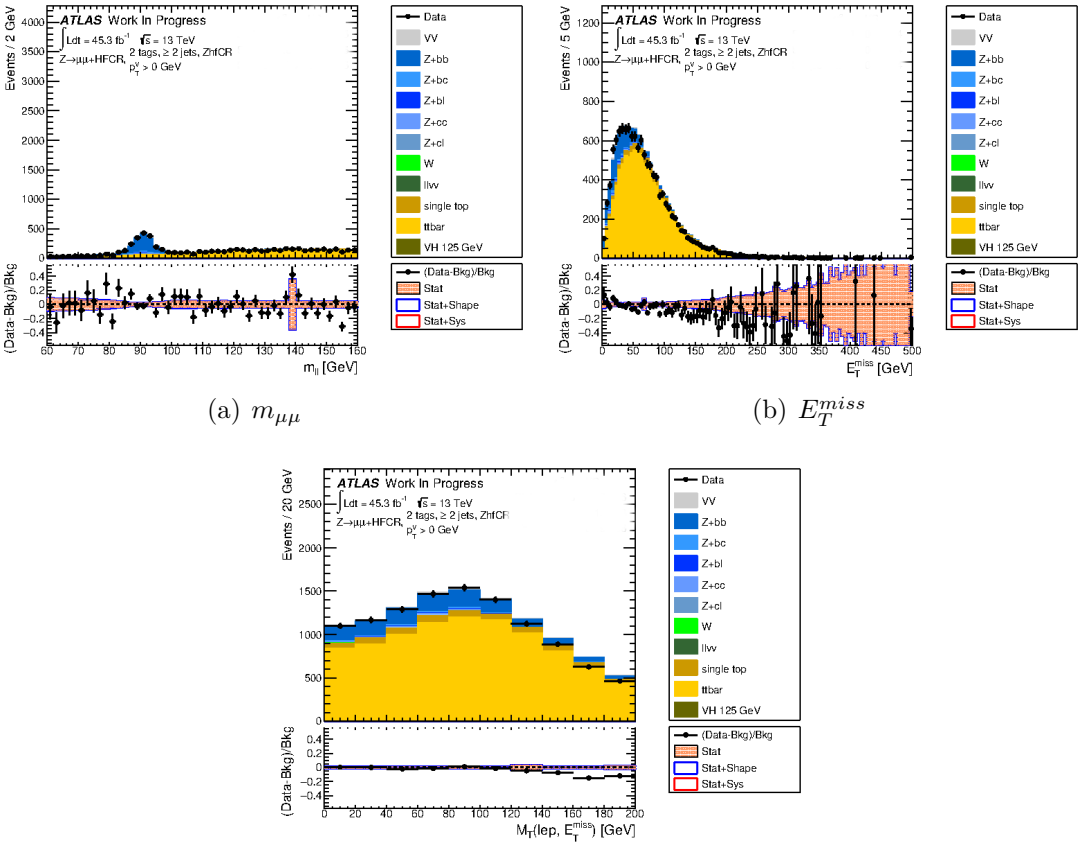

(a) $m_{\mu\mu}$

(b) E_T^{miss}

(c) M_T

Figure A.8.: Different variables plotted from hadhad2 event selection. These plots have been rescaled with $SF(Zbb) = 1.25$ and $SF(t\bar{t}) = 0.99$. The MC used to simulate $Z + h.f.$ events is SHERPA.

Bibliography

[1] S. L. Glashow, *Partial-symmetries of weak interactions*, Nuclear Physics **22(4)**, 579 (1961)

[2] P. W. Higgs, *Broken Symmetries and the Masses of Gauge Bosons*, Phys. Rev. Lett. **13**, 508 (1964)

[3] G. Arnison, et al. (UA1), *Experimental Observation of Isolated Large Transverse Energy Electrons with Associated Missing Energy at s**(1/2) = 540-GeV*, Phys. Lett. **B122**, 103 (1983), [611(1983)]

[4] G. Arnison, et al. (UA1), *Experimental Observation of Lepton Pairs of Invariant Mass Around 95-GeV/c**2 at the CERN SPS Collider*, Phys. Lett. **B126**, 398 (1983), [7.55(1983)]

[5] G. Aad, et al. (ATLAS), *Observation of a new particle in the search for the Standard Model Higgs boson with the ATLAS detector at the LHC*, Phys. Lett. **B716**, 1 (2012), 1207.7214

[6] *Retrieved on 20.07.2019*, URL https://www.kisspng.com/png-particle-physics-standard-model-elementary-particl-4775298/

[7] G. Bhattacharyya, *A Pedagogical Review of Electroweak Symmetry Breaking Scenarios*, Rept. Prog. Phys. **74**, 026201 (2011)

[8] M. Thomson, *Modern Particle Physics*, Cambridge University Press (2013)

[9] G. Altarelli, *A QCD primer*, AIP Conf. Proc. **631(1)**, 70 (2002), hep-ph/0204179

[10] G. Ecker, *Quantum chromodynamics*, in *High-energy physics. Proceedings, European School, Kitzbuehel, Austria, August 21-September, 2005* (2006), hep-ph/0604165

[11] W. de Boer (CMS), *The Discovery of the Higgs Boson with the CMS Detector and its Implications for Supersymmetry and Cosmology*, in *Time and Matter 2013 (TAM2013) Venice, Italy* (2013), 1309.0721

[12] C. Arroyo, B. King, K. Bachmann, A. Bazarko, T. Bolton, C. Foudas, W. Lefmann, W. Leung, S. Mishra, E. Oltman, P. Quintas, S. Rabinowitz, F. Sciulli, W. Seligman, M. Shaevitz, F. Merritt, M. Oreglia, B. Schumm, R. Bernstein, W. Smith, *Precise measurement of the weak mixing angle in neutrino-nucleon scattering.*, Physical review letters **72**, 3452 (1994)

[13] M. T. et al. (Particle Data Group), *Status of Higgs Boson Physics* `Phys.Rev.D98, 030001(2018)`

[14] *Retrieved on 20.07.2019*, URL `https://twiki.cern.ch/twiki/bin/view/LHCPhysics/LHCHXSWGCrossSectionsFigures`

[15] J. R. Andersen, et al. (LHC Higgs Cross Section Working Group), *Handbook of LHC Higgs Cross Sections: 3. Higgs Properties* (2013), `1307.1347`

[16] D. de Florian, et al. (LHC Higgs Cross Section Working Group), *Handbook of LHC Higgs Cross Sections: 4. Deciphering the Nature of the Higgs Sector* (2016), `1610.07922`

[17] C. Lefevre, *The CERN accelerator complex. Complexe des accelerateurs du CERN* (2008), URL `https://cds.cern.ch/record/1260465`

[18] G. Aad, et al. (ATLAS), *Studies of the performance of the ATLAS detector using cosmic-ray muons*, Eur. Phys. J. **C71**, 1593 (2011), `1011.6665`

[19] G. Aad, et al. (ATLAS), *The ATLAS Experiment at the CERN Large Hadron Collider*, JINST **3**, S08003 (2008)

[20] A. Ruiz-Martinez, A. Collaboration, *The Run-2 ATLAS Trigger System*, Technical Report ATL-DAQ-PROC-2016-003, CERN, Geneva (2016), URL `https://cds.cern.ch/record/2133909`

[21] J. Baglio, A. Djouadi, R. Groeber, M. M. Muehlleitner, J. Quevillon, M. Spira, *The measurement of the Higgs self-coupling at the LHC: theoretical status*, JHEP **04**, 151 (2013), `1212.5581`

[22] G. C. Branco, P. M. Ferreira, L. Lavoura, M. N. Rebelo, M. Sher, J. P. Silva, *Theory and phenomenology of two-Higgs-doublet models*, Phys. Rept. **516**, 1 (2012), `1106.0034`

[23] M. e. a. Aaboud (ATLAS), *Search for resonant and non-resonant Higgs boson pair production in the $b\bar{b}\tau^+\tau^-$ decay channel in pp collisions at $\sqrt{s} = 13$ TeV with the ATLAS detector*, Phys. Rev. Lett. **121(19)**, 191801 (2018), [Erratum: Phys. Rev. Lett.122,no.8,089901(2019)], 1808.00336

[24] T. A. collaboration (ATLAS), *Combination of searches for Higgs boson pairs in pp collisions at 13 TeV with the ATLAS experiment.* (2018)

[25] S. Alioli, P. Nason, C. Oleari, E. Re, *A general framework for implementing NLO calculations in shower Monte Carlo programs: the POWHEG BOX*, JHEP **06**, 043 (2010), 1002.2581

[26] T. Sjostrand, S. Mrenna, P. Z. Skands, *A Brief Introduction to PYTHIA 8.1*, Comput. Phys. Commun. **178**, 852 (2008), 0710.3820

[27] T. Gleisberg, S. Hoeche, F. Krauss, M. Schoenherr, S. Schumann, F. Siegert, J. Winter, *Event generation with SHERPA 1.1*, Journal of High Energy Physics **2009(02)**, 007 (2009), URL https://doi.org/10.1088%2F1126-6708%2F2009%2F02%2F007

[28] E. Bothmann, et al., *Event Generation with SHERPA 2.2* (2019), 1905.09127

[29] J. Alwall, M. Herquet, F. Maltoni, O. Mattelaer, T. Stelzer, *MadGraph 5 : Going Beyond*, JHEP **06**, 128 (2011), 1106.0522

[30] URL https://root.cern/doc/master/classTFractionFitter.html

Acknowledgments

First of all, I wanted to thank Prof. Dr. Stan Lai for giving me the opportunity to write my bachelor's thesis in the II. Institute of Physics in Göttingen. All the experiences in the past 14 weeks were incredible and I felt very welcomed throughout this time. The supervision I got was really extraordinary. Thanks to him and his group, I learned a lot about particle physics, experimental methods and working in the physical field and research in general.
Big shout-outs go to Dr. Tobias Bisanz and Petar Bokan, who always supported me, no matter the day and time. They always treated me with a lot of respect, regardless of how many simple questions I had. It was a great pleasure working with you two.
A huge thank you goes to Michael, who always listened to my monologues about this thesis and all my problems that I encountered. You helped me whenever you could, although you were writing your thesis as well. Thanks a lot for that! You are the best friend one could ever wish for.
Finally, I want to thank all my friends and fellow students, that made all this time during my bachelor's studies here in Göttingen to the greatest time imaginable.

Zu guter Letzt möchte ich meiner ganzen Familie noch danken, insbesondere meiner Mama und Rainer, die immer daran geglaubt haben, dass ich das schaffen kann. Ihr standet mir immer zu Rat und Tat zur Seite und hattet immer ein Ohr für mich frei, wenn ich gestresst war. Ohne euch wäre diese Arbeit gar nicht möglich gewesen. Ihr seid die besten Eltern, die man haben kann.

Erklärung nach §13(9) der Prüfungsordnung für den Bachelor-Studiengang Physik und den Master-Studiengang Physik an der Universität Göttingen:

Hiermit erkläre ich, dass ich diese Abschlussarbeit selbständig verfasst habe, keine anderen als die angegebenen Quellen und Hilfsmittel benutzt habe und alle Stellen, die wörtlich oder sinngemäß aus veröffentlichten Schriften entnommen wurden, als solche kenntlich gemacht habe.
Darüberhinaus erkläre ich, dass diese Abschlussarbeit nicht, auch nicht auszugsweise, im Rahmen einer nichtbestandenen Prüfung an dieser oder einer anderen Hochschule eingereicht wurde.

Göttingen, den 23. Oktober 2019

(Vanessa Annabelle Grauer)